arXiv:2303.01174v1 [astro-ph.HE] 2 Mar 2023

Astronomical puzzle Cyg X-3 is a hidden Galactic ultraluminous X-ray source

Alexandra Veledina[1,2*], Fabio Muleri[3], Juri Poutanen[1], Jakub Podgorný[4,5,6], Michal Dovčiak[5], Fiamma Capitanio[3], Eugene Churazov[7,8], Alessandra De Rosa[3], Alessandro Di Marco[3], Sofia Forsblom[1], Philip Kaaret[9], Henric Krawczynski[10], Fabio La Monaca[3], Vladislav Loktev[1], Alexander A. Lutovinov[8], Sergey V. Molkov[8], Alexander A. Mushtukov[11], Ajay Ratheesh[3], Nicole Rodriguez Cavero[10], James F. Steiner[12], Rashid A. Sunyaev[7,8], Sergey S. Tsygankov[1], Andrzej A. Zdziarski[13], Stefano Bianchi[14], Joe S. Bright[11], Nikolaj Bursov[15], Enrico Costa[3], Elise Egron[16], Javier A. Garcia[17], David A. Green[18], Mark Gurwell[12], Adam Ingram[19], Jari J. E. Kajava[1,20], Ruta Kale[21], Alex Kraus[22], Denys Malyshev[23], Frédéric Marin[4], Giorgio Matt[14], Michael McCollough[12], Ilia A. Mereminskiy[8], Nikolaj Nizhelsky[15], Giovanni Piano[3], Maura Pilia[16], Carlotta Pittori[24,25], Ramprasad Rao[12], Simona Righini[26], Paolo Soffitta[3], Anton Shevchenko[15], Jiri Svoboda[5], Francesco Tombesi[27,28,29], Sergei Trushkin[15,30], Peter Tsybulev[15], Francesco Ursini[14], Martin C. Weisskopf[9], Kinwah Wu[31], Iván Agudo[32], Lucio A. Antonelli[25,24], Matteo Bachetti[16], Luca Baldini[33,34], Wayne H. Baumgartner[9], Ronaldo Bellazzini, Stephen D. Bongiorno[9], Raffaella Bonino[35,36], Alessandro Brez[33], Niccolò Bucciantini[37,38,39], Simone Castellano[33], Elisabetta Cavazzuti[40], Chien-Ting Chen[41], Stefano Ciprini[28,24], Ettore Del Monte[3], Laura Di Gesu[40], Niccolò Di Lalla[42], Immacolata Donnarumma[40], Victor Doroshenko[23], Steven R. Ehlert[9], Teruaki Enoto[43], Yuri

Evangelista[3], Sergio Fabiani[3], Riccardo Ferrazzoli[3], Shuichi Gunji[44], Kiyoshi Hayashida[45], Jeremy Heyl[46], Wataru Iwakiri[47], Svetlana G. Jorstad[48,49], Vladimir Karas[5], Fabian Kislat[50], Takao Kitaguchi[43], Jeffery J. Kolodziejczak[9], Luca Latronico[35], Ioannis Liodakis[51], Simone Maldera[35], Alberto Manfreda[33], Andrea Marinucci[40], Alan P. Marscher[48], Herman L. Marshall[52], Francesco Massaro[35,36], Ikuyuki Mitsuishi[53], Tsunefumi Mizuno[54], Michela Negro[55,56,57], Chi-Yung Ng[58], Stephen L. O'Dell[9], Nicola Omodei[42], Chiara Oppedisano[35], Alessandro Papitto[25], George G. Pavlov[59], Abel L. Peirson[42], Matteo Perri[24,25], Melissa Pesce-Rollins[33], Pierre-Olivier Petrucci[60], Andrea Possenti[16], Simonetta Puccetti[24], Brian D. Ramsey[9], John Rankin[3], Oliver Roberts[41], Roger W. Romani[42], Carmelo Sgrò[33], Patrick Slane[12], Gloria Spandre[33], Doug Swartz[41], Toru Tamagawa[43], Fabrizio Tavecchio[61], Roberto Taverna[62], Yuzuru Tawara[53], Allyn F. Tennant[9], Nicholas E. Thomas[9], Alessio Trois[16], Roberto Turolla[62,31], Jacco Vink[63], Fei Xie[64,3] and Silvia Zane[31]

[1]Department of Physics and Astronomy, FI-20014 University of Turku, Finland.
[2]Nordita, KTH Royal Institute of Technology and Stockholm University, Hannes Alfvéns väg 12, SE-106 91, Sweden.
[3]INAF Istituto di Astrofisica e Planetologia Spaziali, Via del Fosso del Cavaliere 100, 00133 Roma, Italy.
[4]Université de Strasbourg, CNRS, Observatoire Astronomique de Strasbourg, UMR 7550, 67000 Strasbourg, France.
[5]Astronomical Institute of the Czech Academy of Sciences, Boční II 1401/1, 14100 Praha 4, Czech Republic.
[6]Astronomical Institute, Charles University, V Holešovičkách 2, 18000 Praha, Czech Republic.
[7]Max Planck Institute for Astrophysics, Karl-Schwarzschild-Str 1, D-85741 Garching, Germany.
[8]Space Research Institute of the Russian Academy of Sciences, Profsoyuznaya Str. 84/32, Moscow 117997, Russia.
[9]NASA Marshall Space Flight Center, Huntsville, AL 35812, USA.
[10]Physics Department and McDonnell Center for the Space Sciences, Washington University in St. Louis, St. Louis, MO 63130, USA.

[11]Astrophysics, Department of Physics, University of Oxford, Denys Wilkinson Building, Keble Road, Oxford OX1 3RH, UK.
[12]Harvard-Smithsonian Center for Astrophysics, 60 Garden St, Cambridge, MA 02138, USA.
[13]Nicolaus Copernicus Astronomical Center, Polish Academy of Sciences, Bartycka 18, PL-00-716 Warszawa, Poland.
[14]Dipartimento di Matematica e Fisica, Università degli Studi Roma Tre, Via della Vasca Navale 84, 00146 Roma, Italy.
[15]Special Astrophysical Observatory of the Russian Academy of Sciences, Nizhnij Arkhyz, 369167, Karachayevo-Cherkessia, Russia.
[16]INAF Osservatorio Astronomico di Cagliari, Via della Scienza 5, 09047 Selargius (CA), Italy.
[17]California Institute of Technology, Pasadena, CA 91125, USA.
[18]Cavendish Laboratory, University of Cambridge, 19 J. J. Thomson Avenue, Cambridge CB3 0HE, United Kingdom.
[19]School of Mathematics, Statistics, and Physics, Newcastle University, Newcastle upon Tyne NE1 7RU, UK.
[20]Serco for the European Space Agency (ESA), European Space Astronomy Centre, Camino Bajo del Castillo s/n, E-28692 Villanueva de la Cañada, Madrid, Spain.
[21]National Centre for Radio Astrophysics, Tata Institute of Fundamental Research, S. P. Pune University Campus, Ganeshkhind, Pune 411007, India.
[22]Max-Planck-Institut für Radioastronomie, Auf dem Hügel 69, D-53121 Bonn, Germany.
[23]Institut für Astronomie und Astrophysik, Universität Tübingen, Sand 1, 72076 Tübingen, Germany.
[24]Space Science Data Center, Agenzia Spaziale Italiana, Via del Politecnico snc, 00133 Roma, Italy.
[25]INAF Osservatorio Astronomico di Roma, Via Frascati 33, 00078 Monte Porzio Catone (RM), Italy.
[26]INAF Institute of Radio Astronomy, Via Gobetti 101, I–40129 Bologna, Italy.
[27]Dipartimento di Fisica, Università degli Studi di Roma "Tor Vergata", Via della Ricerca Scientifica 1, 00133 Roma, Italy.
[28]Istituto Nazionale di Fisica Nucleare, Sezione di Roma "Tor Vergata", Via della Ricerca Scientifica 1, 00133 Roma, Italy.
[29]Department of Astronomy, University of Maryland, College Park, Maryland 20742, USA.

[30]Kazan Feferal University, Kremlyovskaya str., Kazan 420008, Tatarstan, Russia.

[31]Mullard Space Science Laboratory, University College London, Holmbury St Mary, Dorking, Surrey RH5 6NT, UK.

[32]Instituto de Astrofísica de Andalucía—CSIC, Glorieta de la Astronomía s/n, 18008 Granada, Spain.

[33]Istituto Nazionale di Fisica Nucleare, Sezione di Pisa, Largo B. Pontecorvo 3, 56127 Pisa, Italy.

[34]Dipartimento di Fisica, Universitã di Pisa, Largo B. Pontecorvo 3, 56127 Pisa, Italy.

[35]Istituto Nazionale di Fisica Nucleare, Sezione di Torino, Via Pietro Giuria 1, 10125 Torino, Italy.

[36]Dipartimento di Fisica, Università degli Studi di Torino, Via Pietro Giuria 1, 10125 Torino, Italy.

[37]INAF Osservatorio Astrofisico di Arcetri, Largo Enrico Fermi 5, 50125 Firenze, Italy.

[38]Dipartimento di Fisica e Astronomia, Università degli Studi di Firenze, Via Sansone 1, 50019 Sesto Fiorentino (FI), Italy.

[39]Istituto Nazionale di Fisica Nucleare, Sezione di Firenze, Via Sansone 1, 50019 Sesto Fiorentino (FI), Italy.

[40]Agenzia Spaziale Italiana, Via del Politecnico snc, 00133 Roma, Italy.

[41]Science and Technology Institute, Universities Space Research Association, Huntsville, AL 35805, USA.

[42]Department of Physics and Kavli Institute for Particle Astrophysics and Cosmology, Stanford University, Stanford, California 94305, USA.

[43]RIKEN Cluster for Pioneering Research, 2-1 Hirosawa, Wako, Saitama 351-0198, Japan.

[44]Yamagata University,1-4-12 Kojirakawa-machi, Yamagata-shi 990-8560, Japan.

[45]Osaka University, 1-1 Yamadaoka, Suita, Osaka 565-0871, Japan.

[46]University of British Columbia, Vancouver, BC V6T 1Z4, Canada.

[47]International Center for Hadron Astrophysics, Chiba University, Chiba 263-8522, Japan.

[48]Institute for Astrophysical Research, Boston University, 725 Commonwealth Avenue, Boston, MA 02215, USA.

[49]Department of Astrophysics, St. Petersburg State University, Universitetsky pr. 28, Petrodvoretz, 198504 St. Petersburg, Russia.

[50]Department of Physics and Astronomy and Space Science Center, University of New Hampshire, Durham, NH 03824, USA.

[51]Finnish Centre for Astronomy with ESO, 20014 University of Turku, Finland.

[52]MIT Kavli Institute for Astrophysics and Space Research, Massachusetts Institute of Technology, 77 Massachusetts Avenue, Cambridge, MA 02139, USA.

[53]Graduate School of Science, Division of Particle and Astrophysical Science, Nagoya University, Furo-cho, Chikusa-ku, Nagoya, Aichi 464-8602, Japan.

[54]Hiroshima Astrophysical Science Center, Hiroshima University, 1-3-1 Kagamiyama, Higashi-Hiroshima, Hiroshima 739-8526, Japan.

[55]University of Maryland, Baltimore County, Baltimore, MD 21250, USA.

[56]NASA Goddard Space Flight Center, Greenbelt, MD 20771, USA.

[57]Center for Research and Exploration in Space Science and Technology, NASA/GSFC, Greenbelt, MD 20771, USA.

[58]Department of Physics, The University of Hong Kong, Pokfulam, Hong Kong.

[59]Department of Astronomy and Astrophysics, Pennsylvania State University, University Park, PA 16802, USA.

[60]Université Grenoble Alpes, CNRS, IPAG, 38000 Grenoble, France.

[61]INAF Osservatorio Astronomico di Brera, Via E. Bianchi 46, 23807 Merate (LC), Italy.

[62]Dipartimento di Fisica e Astronomia, Università degli Studi di Padova, Via Marzolo 8, 35131 Padova, Italy.

[63]Anton Pannekoek Institute for Astronomy & GRAPPA, University of Amsterdam, Science Park 904, 1098 XH Amsterdam, The Netherlands.

[64]Guangxi Key Laboratory for Relativistic Astrophysics, School of Physical Science and Technology, Guangxi University, Nanning 530004, China.

*Corresponding author(s). E-mail(s):
alexandra.veledina@gmail.com;

Abstract

How black holes consume and eject matter has been the subject of intense studies for more than 60 years. The luminosity of these systems are often compared to the Eddington limit, the border at which the spherical accretion is inhibited by the radiation pressure of photons it produces. The discovery of ultraluminous X-ray sources (ULXs) showed that accretion can proceed even when the apparent luminosity exceeds the Eddington limit [1]. High apparent luminosity might be produced by the beaming of the incident radiation by a thick collimated outflow or by a truly super-Eddington accretion flow. However, possibilities to study these outflows in detail are limited, as ULXs are typically found in distant galaxies. Using the Imaging X-ray Polarimetry Explorer (IXPE) [2], we made the first measurement of X-ray polarization in Galactic X-ray binary Cyg X-3. The detection of high, $\approx25\%$, nearly energy-independent linear polarization, orthogonal to the direction of the radio ejections, unambiguously indicates the primary source is obscured and the observer on Earth only sees reflected and scattered light. Modelling shows there is an optically thick envelope with a narrow funnel around the primary X-ray source in the system. We derive an upper limit on the opening angle of the funnel that implies a lower limit on the beamed luminosity exceeding the Eddington value. We show that Cyg X-3 is viewed as a ULX to an extragalactic observer located along the axis of the funnel. Our findings reveal this unique persistent source as an ideal laboratory for the study of the inner workings of ULX central engines.

1 Main

Cyg X-3 is one of the first sources discovered in the X-ray sky [3]. It is the brightest X-ray binary in radio wavelengths [4, 5], with peak fluxes reaching ~10 Jy, and one of the few X-ray binaries where γ-ray emission has been detected [6, 7]. Cyg X-3 is also exceptional from the point of view of population synthesis and evolutionary studies [8, 9]. It is the only known Galactic source containing a compact object in a binary orbit with a Wolf-Rayet (WR) star – an evolved massive star that ran out of its hydrogen fuel [10, 11]; it is the progenitor of a double-degenerate system [9] that will become a source of gravitational wave emission in the distant future.

The optical counterpart is not visible because of the high absorption along the line of sight: the source is located in the Galactic plane at a distance $D = 7.4 \pm 1.1$ kpc [12]. The system parameters have been constrained based on radio, X-ray and infrared properties. Spatially resolved discrete radio ejections [13, 14] are aligned in the north-south direction. Moreover, the position angle
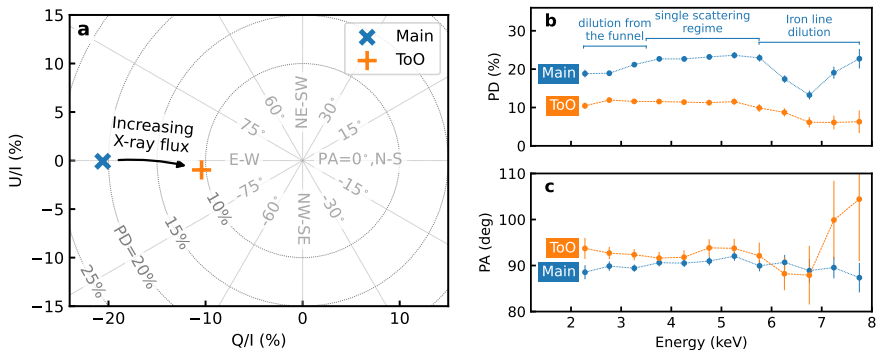
Fig. 1 Orbital-phase averaged polarization properties. (a) Normalized Stokes parameters Q/I–U/I for the Main and ToO observations. The energy dependence of the average PD **(b)** and PA **(c)**.

of the intrinsic infrared polarization (likely coming from scattering off the circumstellar disc [15]) agrees with the jet position angle. The orbital period $P_{\rm orb} = 4.8^{\rm h}$ has been measured with high accuracy based on the prominent X-ray and infrared (IR) flux modulations, as well as from the periodic Doppler shifts of the X-ray and IR lines [16–19], and is known to increase rapidly over time [20, 21]. The analysis of the Doppler shifts of X-ray lines [18] imply an orbital inclination of $i = 38° \pm 12°$; this estimate depends on the assumed mass of the WR star. The detection of the one-sided jet [22], which is thought to be the Doppler-boosted approaching jet, suggests an angle to jet axis $i_{\rm j} < 14°$. A similar value, $i_{\rm j} = 10°.5 \pm 4°.2$, was inferred from observations of two-sided ejections [14]. Recent analysis of the orbital photometric variations in X-rays and IR [23] gave consistently small orbital inclination, $i \approx 30°$.

The source swings between several X-ray spectral states, tightly linked to radio properties ([24] and Fig. A4 in Methods A). The source spends most of the time in the hard X-ray, quiescent radio state. The high-energy emission can be described by a power law with prominent fluorescent iron lines (Fig. A6 and Methods A). Occasionally, Cyg X-3 shows transitions to an ultrasoft spectral state, during which the spectrum is dominated by a blackbody peaking at a few keV. Transitions to this state are accompanied by major radio ejections, in which the highest observed radio fluxes are reached. The spectral transitions are thought to be related to changes of accretion geometry, however, the exact geometrical configuration and physical reasons behind the changes are not known.

Understanding the physical picture of the system is complicated by the diversity of models that can explain the X-ray spectra: the quiescent-state spectra can be well fitted with either (i) an intrinsically soft spectrum severely absorbed in the WR wind, or (ii) with a hard spectrum coming from the hot medium located within the truncated cold accretion disc (this model is often discussed in the context of other hard-state sources), or (iii) with the equal contribution of the incident spectrum and the reflected emission [25, 26]. The

models invoke very different emission mechanisms and a wide range of inherent luminosities and accretion rates, preventing us from identifying the accretion-ejection mechanisms of this unusual binary. The astronomical puzzle called Cyg X-3 [16] remained unsolved for over 50 years after its discovery, even though the system is one of the best studied sources in the X-ray sky.

We report here on the first detection of the X-ray polarization from Cyg X-3. Observations with the IXPE satellite allowed to pinpoint the accretion-ejection geometry of the source. The first IXPE observation (here-after referred to as "Main") caught the source in the hard X-ray (radio-quiescent) state and consisted of two runs, 14–19 October 2022 and 31 October–6 November 2022. We detect a high polarization degree PD=20.6 ± 0.3% in the 2–8 keV range (see Fig. 1a). The polarization angle PA=90°.1 ± 0°.4 (that is determined by the direction of electric field oscillations, measured from north through east on the sky) is orthogonal to the position angle of the discrete radio ejections and the infrared and sub-mm polarization ([13–15] and Table A4). The observed PD is constant over the 3.5–6 keV range, but decreases in the 6–8 keV energy range, where the fluorescent Fe Kα emission line dominates, and below 3 keV.

We performed spectro-polarimetric modelling (see Methods A.1) with a model similar to that used for ULXs [1]. The model consists of a dominant broken power-law component, a thermal component at low energies, and emission from the iron line complex near 6.4 keV. The break in the power-law component is seen at energies consistent with those seen in ULXs [1]. The thermal component is modelled as multi-temperature blackbody emission but interpreted (see below) as emission from the funnel, similar to the interpretation for ULXs. IXPE reveals that the power-law component is highly polarized with constant PD=24.9 ± 0.7%; this suggests that it is likely due to reflection. The thermal component has at most low polarization and the line emission is unpolarized.

We performed an orbital phase-resolved analysis of the polarimetric data using the recent ephemeris ([21], see Methods A.1). We note large variations of the PA (Fig. 2). The pattern is not consistent with the simple model of scattering off optically-thin plasma [27], e.g. scattering off the wind of the WR star. In this case, the low inclination of the system would lead to a sinusoidal variations of PA with two peaks per orbital period (equivalent to a double loop in the normalized Stokes parameters Q/I–U/I plane). Furthermore, the PD of the primary X-rays reflected off the star is expected to be <1%, due to the small solid angle subtended by the star as seen from the compact object. For a higher solid angle of the scattering matter, namely if scattering proceeds in the WR wind, a low PD is also expected, as in this case the scatterers are nearly spherically symmetric. The high average PD, ≈ 25%, and its orientation relative to the radio outflows suggest that the IXPE signal is dominated by the reflected component, with minor to zero contribution of the primary continuum. This conclusion is bolstered by our finding of a largely energy-independent polarization as the superposition of comparable contributions of
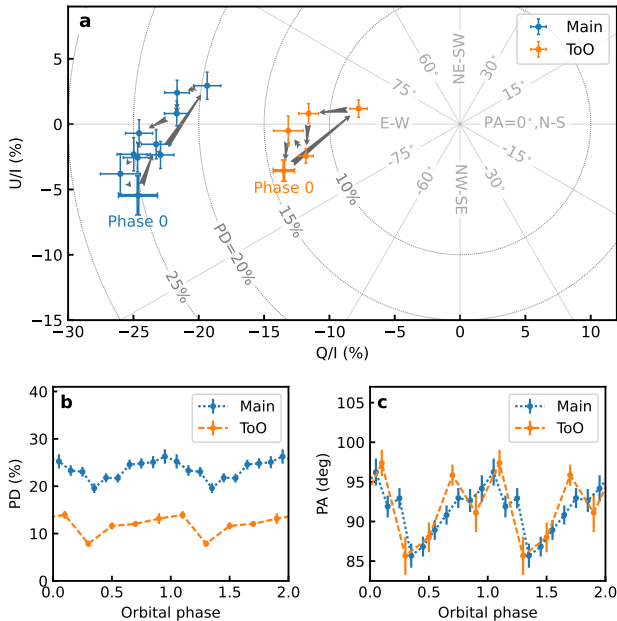
Fig. 2 Orbital phase-folded polarization properties. (a) Evolution of the normalized Stokes parameters Q/I–U/I. The dependence of the PD **(b)** and PA **(c)** on the orbital phase in the 3.5–6 keV energy range.

primary and reflected emission would lead to a strong energy dependence of the PD. The observed broadband spectral energy distribution (SED) is also consistent with pure reflection of an intrinsically rather soft spectrum (see Methods A.2).

The polarization of Cyg X-3 resembles closely that of the accreting super-massive black hole in the Circinus galaxy which exhibits a PD of $28 \pm 7\%$ [28]. In this source, the primary X-rays are believed to be obscured by a dusty torus with an inclination exceeding that of the host galaxy, $i \sim 65°$, so that the reflected emission dominates over the direct emission in the IXPE band. This finding leads to an important implication for the accretion geometry of Cyg X-3: as the observer at $i \sim 30°$ [18, 22, 23] does not see the primary X-ray source, we infer the presence of an optically thick medium shaped as a funnel. For the Thomson scattering law, the observed PD translates to the typical scattering angle $\approx 38°$, which is close to the orbital inclination. Our modelling indicates a very narrow funnel with a $\lesssim 16°$ half-opening angle, see Fig. 3.

Optically thick and elevated envelopes are hallmarks of super-Eddington accretion rates [29, 30]. We can check this hypothesis by estimating the intrinsic X-ray luminosity of Cyg X-3. Assuming that the observed radiation comes from the visible inner part of the funnel, we can relate the reflected luminosity to the intrinsic one through the reflection albedo and the solid angle of the visible part of the funnel (alternatively, the scattering can proceed in the WR wind right above the funnel, but the resulting luminosities are the same, see more details
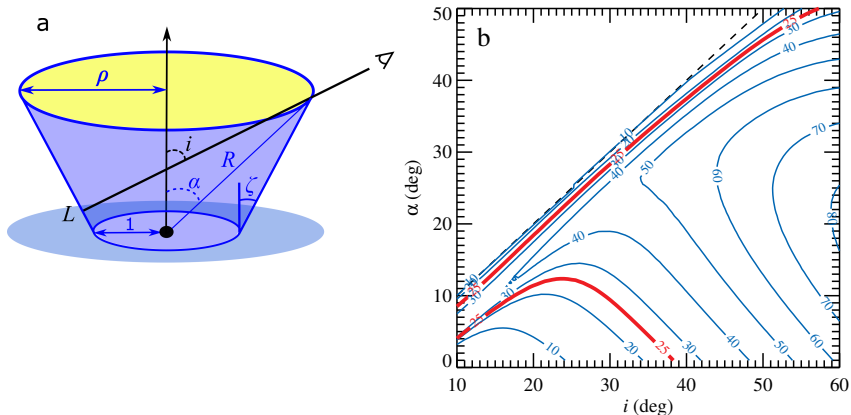
Fig. 3 Geometry of the funnel and its polarization properties. (a) Proposed geometry of the funnel with the emitting source marked by a black circle. **(b)** Contour plots of the constant PD for different observer inclinations i and opening angles of the funnel α. Red contour marks the observed polarization of 25%.

in Methods A). We find that the intrinsic luminosity exceeds the Eddington limit for a neutron star accretor at opening angles $\alpha \approx 8°$, while for $\alpha \approx 16°$ this limit is exceeded even for a black hole of 20 solar masses. Further, for the small opening angle of the funnel required by polarimetric data, the apparent luminosity for an observer viewing down the funnel is $L \gtrsim 5 \times 10^{39}$ erg s^{-1} in 2–8 keV range, which puts Cyg X-3 in the class of ULX sources.

With the aim to identify the properties of the accretion geometry that drive the soft-hard-state transitions, we performed an additional IXPE target of opportunity ("ToO" hereafter) observation as the source transitioned towards the soft state (as indicated by the X-ray and radio fluxes, see Methods A.2) on 25–29 December 2022. The ToO revealed a twice lower, largely energy-independent PD=10.4±0.3% at 2–8 keV with a PA=92°.6±0°.7, which is similar to the value found in the Main observation (see orange symbols in Figs. 1–2). This suggests that we continue seeing the reflected signal in this state, but the funnel parameters have changed, in particular, the decreased polarization may suggest the reflection and reprocessing now operates in some volume of matter around the funnel, rather than coming solely from its surface. This is consistent with the outflow becoming more transparent. We expect that the subsequent drop of the accretion rate will lead to a collapse of the funnel, revealing the X-ray emission from the inner parts of the accretion disc, accompanied by the drop of its polarization. In this scenario, the ultrasoft Cyg X-3 emission would correspond to a lower accretion rate when compared to the hard X-ray/radio quiescent state, even though the source appears brighter. Following our findings, the whole complex of multiwavelength properties may need to be reconsidered in terms of the new physical scenario.

The X-ray polarimetric data probe, for the first time, the accretion geometry in Cyg X-3, allowing to better understand the physical nature of the source. These data have revealed that this famous and long-studied Galactic

source has been silently accreting in the super-Eddington regime. This discovery opens a new chapter in the study of this exceptional source, and establishes it as an analogue of distant ULXs. The geometry and dynamics of the accretion flow of supper-Eddington ULXs can now be studied in much greater detail using this bright and persistent Galactic counterpart.

Author contributions.   A.V. led the modelling of the data and the writing of the paper. F.Mu. led the analysis of the IXPE data. Ju.Pou. led the analytical modelling and contributed to writing of the paper. Ja.Pod. performed Monte-Carlo simulations supporting the modelling. M.D. led the work of the IXPE Topical Working Group on Accreting stellar-mass black holes. A.D.R., E.Ch., P.K. and R.A.S. contributed with parts of the paper and its content. F.C., A.D.M, S.F., H.K., F.L.M., A.A.L., S.V.M., A.R., N.R.C., J.F.S., S.S.T., A.A.Z. and J.J.E.K., I.A.M., G.P. and C.P. contributed to planning, reducing and analysing the X-ray/gamma-ray data. V.L., A.A.M. and D.M. contributed to analytical estimates and modelling. J.S.B., N.B., E.E., D.A.G., M.G., R.K., A.K., M.McC., N.N., M.P., R.R., S.R., A.S., J.S., S.T. and P.T. contributed with radio/sub-millimeter data. S.B., E.Co., J.A.G., A.I., F.M., G.M., P.S., F.T., F.U., M.W. and K.W. contributed with discussion of methods and conclusions. The remaining authors have contributed to the design, science case of the IXPE mission and planning of observations relevant to the present paper.

Competing interest.   Authors declare that they have no competing interests.

Data availability.   The IXPE, Nustar, INTEGRAL and Fermi data are freely available in the HEASARC IXPE Data Archive (https://heasarc.gsfc.nasa.gov). The multiwavelength data are available on request from the individual observatories.

Code availability.   The analysis and simulation software IXPEOBSSIM developed by IXPE collaboration and its documentation is available publicly through the web-page https://ixpeobssim.readthedocs.io/en/latest/?badge=latest.494. XSPEC is distributed and maintained under the aegis of the HEASARC and can be downloaded as part of HEAsoft from http://heasarc.gsfc.nasa.gov/docs/software/lheasoft/download.html. MIR software package for SMA data: https://lweb.cfa.harvard.edu/~cqi/mircook.html.

Appendix A   Methods

A.1   X-ray polarization data and analysis

An attempt to detect the linear polarization of the X-rays from Cyg X-3 was made with the OSO-8 satellite [31], but the presence of other bright sources in the field of view prevented the authors to reach firm conclusions. IXPE [2] observed Cyg X-3 twice: the first and second observations were named "Main" and "ToO". The Main observation was split in two observing periods close in time: the first started on 2022-10-14 01:26:33 UTC and ended on 2022-10-19 14:12:56 UTC, and the second was carried out between 2022-10-31 12:50:08 UTC and 2022-11-06 08:42:21 UTC. The ToO observation started on 2022-12-25 10:05:17 UTC and ended on 2022-12-29 17:44:22 UTC. The livetime of the Main and ToO observation is ~538 ks and ~199 ks, respectively.

The analysis of the IXPE data was carried out similarly to other observations (e.g., see [32]). Level 2 (processed) data were downloaded from the IXPE HEASARC archive. These data consist of three photon lists, one for each of the IXPE telescopes, and contain for each collected photon the time, position in the sky, as well as the Stokes parameters of the single event. The arrival time of the photons were corrected to the Solar system barycenter using the barycorr tool from the FTOOLS package, included in HEASOFT version 6.31, using the Jet Propulsion Laboratory (JPL) Development Ephemeris (DE421) and the International Celestial Reference System (ICRS) reference frame.

The source extraction region with a radius of 90 arcsec was centered on the source position. We *did not* attempt to extract the background from the remaining part of the field of view and subtract it from the source signal, because the background in the IXPE field of view for relatively bright sources like Cyg X-3 is relatively weak and is dominated by the contamination of the source photons which are focused in the outer wings of the mirror Half Power Diameter (HPD) [33]. Thus, removing the background in this case mostly removes several per cent of the source signal.

Polarization can be obtained from the IXPE photon list with two approaches. The first is building the Stokes spectra $I(E)$, $Q(E)$ and $U(E)$, which are calculated by summing the relevant Stokes parameter for all the events in a specific energy bin. Such spectra can then be fitted with a forward-fitting software, associating for each spectral component a certain polarization model [34]; in our case, we used XSPEC version 12.13.0 [35]. The second approach relies on the use of IXPEOBSSIM package [36], which calculates the Stokes parameters as the sum of the event values in a certain energy, time or angular bin [37]. The latter approach does not assume any underlying model. Data collected from the three IXPE telescopes were analysed separately, applying the appropriate response matrices (unweighted, version 12, in our case) which are available at the HEASARC CALDB and in the IXPEOBSSIM package.

Average polarization in the entire IXPE energy range (2–8 keV) was calculated with the PCUBE algorithm included in the IXPEOBSSIM/XPBIN tool. The PD=20.6 ± 0.3% and 10.4 ± 0.03% were found for the Main and ToO observations, respectively, with a PA=90°.1 ± 0°.4 and PA=92°.6 ± 0°.7, measured east of north.

It is well-known that the spectrum of Cyg X-3 has a wealth of spectral features, which are also variable with time and orbital phase [19]. To model the average I, Q and U spectra obtained by IXPE, we adopt a relatively simple and phenomenological model with the aim of capturing the relation between the main spectral components and their polarization, which is the scope of this paper. Our basic model comprises of an absorbed broken power law, a gaussian, broad, line which represents the prominent Iron complex at about 6.5 keV, and a thermal component described by the multi-temperature accretion disc. A constant polarization was associated to each of these components; abundances are from [38]. In addition to these main components, we added four gaussian lines, either in emission or in absorption, to account for the known

strongest spectral features of Cyg X-3 that are appreciated also in the IXPE spectra. The energy of these lines is fixed at the value observed in the NICER spectrum (see Figure A6) and their intrinsic width is also frozen to 0.15 keV. It is worth noting that such features can be identified only in the I spectrum, whereas their contributions to the Q and U spectra (and then to polarization) is not recognizable with the sensitivity of the IXPE measurement; therefore, all of these components are assumed to be completely unpolarized. As IXPE observed Cyg X-3 in a relatively bright state for a long time, the large collected number of events made evident small systematic difference among the three IXPE telescopes, again affecting significantly only the I spectrum. To account for them, we introduced a Multiplicative Power Law (MPL) cross-calibration function which reads $f \times E^\gamma$, similarly to what was done for the black hole Cyg X-1 observed by IXPE [32]. The first IXPE telescope was taken as a reference, and therefore for this detector we froze $f = 1$ and $\gamma = 0$. The complete XSPEC model then reads TBABS×[POLCONST×GAUSSIAN + POLCONST×BKNPOWER + POLCONST×DISKBB + (GAUSSIAN + GAUSSIAN + GAUSSIAN + GAUSSIAN)]×MPL.

Spectro-polarimetric modelling for the Main and ToO observations is shown in Figure A1 and model parameters are reported in Table A1. For both the Main and ToO observations, the polarization of the prominent line associated to the complex of neutral iron is unpolarized, to account for the large reduction of measured PD at those energies. The broken power law is highly polarized, ~25% for the Main observation and ~12% for the ToO, with a break at ~6 keV which is in line with other ULXs [1]. The thermal component is not required in the spectral fitting alone, but its nearly-unpolarized contribution is required to account for the measured decrease of PD at lower energies observed in the Main observation. Such a decrease is not observed during the ToO, and indeed the polarization of the thermal component remains essentially not determined for this observation.

It is well known that Cyg X-3 exhibits a large modulation in flux with the orbital phase of the binary system [20, 23]. To investigate possible variations in polarization, we folded the IXPE observations of the source with the ephemeris in Table 2 (2nd model) of [21]. Phase 0 identifies the superior conjunction of the system, in which the compact object is behind the WR star. Data were grouped in 10 (5) phase bins for the Main (ToO) observation and polarization was calculated with the IXPEOBSSIM/XPBIN algorithm in three energy bands, 2–3.5, 3.5–6 and 6–8 keV. These were chosen to highlight, in the energy range of IXPE, the contributions of the main spectral features identified in the spectro-polarimetric modelling, which are: the thermal component described by multi-temperature accretion disc at low energy, the broken power law at intermediate energies, and the iron line complex in the highest energy bin. The phase-folded PD and PA are shown in Figure A2, and they show evident orbital variations. PA variations are nearly sinusoidal with an amplitude of ~ ±5°, in both the Main and ToO observations, while PD variations are more irregular with an amplitude of a few percent. The average PD measured in the ToO is a factor
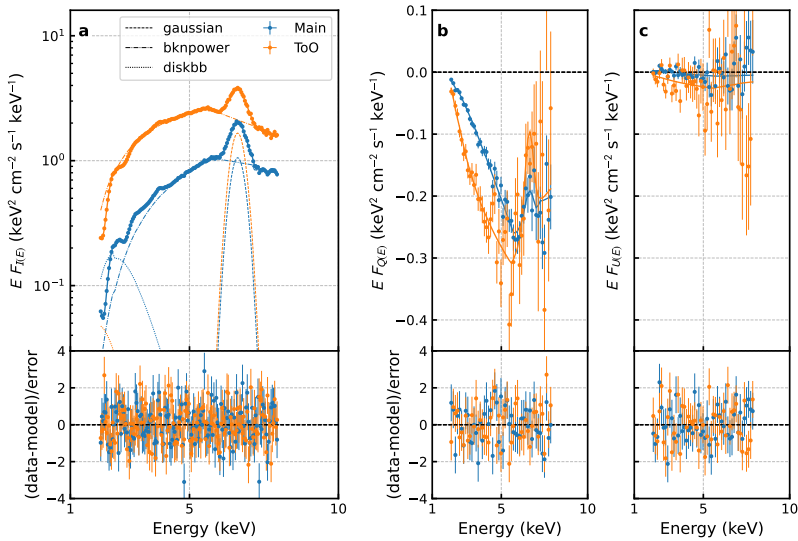
Fig. A1 Average spectropolarimetric data with the best-fitting model. The Stokes parameters I **(a)**, Q **(b)** and U **(c)** (photon fluxes multiplied by energy) as a function of photon energy. Only the contribution of the main spectral components are shown in **a** for graphical clarity.

of two lower with respect to the Main observation, and shows similar but not identical orbital profiles.

It is worth noting that, excluding variations due to orbital phase, polarization remains stable over time. This is shown in Figure A3, where we compare the measured polarization degree and angle in the total IXPE energy range, binned with time bins of one period, with flux and hardness ratio variations during the IXPE Main observation. While the latter are varying significantly, PD and PA varies around the average value essentially within statistical uncertainties. This suggests that the geometry which defines the high polarization observed for Cyg X-3 is stable with time and essentially unrelated to the ultimate mechanisms producing X-ray variability at superorbital timescales.

A.2 Multiwavelength observations

Cyg X-3 has been frequently observed over the past decades from radio through γ-rays. On long, weeks to months, time-scales, the source evolves through the sequence of distinct X-ray and radio spectral states (see Fig. A4 and [24, 39]). The most frequent state is the hard X-ray, radio quiescent state, which corresponds to the lowest observed X-ray flux. We observed the source in this state during the Main IXPE run (Fig. A5). The absorption within the binary is uncertain, hence different branches of spectral models, corresponding to different geometries and dominant spectral components, have been proposed [25, 26], including the models where the incident power-law-like Comptonization spectrum is heavily absorbed or down-scattered in the stellar wind, models

Table A1 Model parameters for the spectropolarimetric fit of the IXPE data only, for the Main and ToO observations. The model reads: TBABS×[POLCONST×GAUSSIAN + POLCONST×BKNPOWER + POLCONST×DISKBB + (GAUSSIAN + GAUSSIAN + GAUSSIAN + GAUSSIAN)]×MPL. Uncertainties are calculated with the XSPEC/ERROR command at 90% confidence level. A multplicative power law (MPL) function accounts for the mutual cross-calibration of the three IXPE telescopes; det1 is taken as reference. Negative (positive) values for the normalization of Gaussian components indicate absorption (emission) lines.

	Main	ToO
$N_{\rm H}$ (10^{22} cm^{-2})	$9.0^{+0.3}_{-2.8}$	$5.0^{+2.9}_{-0.4}$
Fe complex gauss. PD (%)	0^{+2}_{-0}	0^{+3}_{-0}
Fe complex gauss. PA (deg)	undefined	undefined
Fe complex gauss. line energy (keV)	6.60 ± 0.02	$6.60^{+0.04}_{-0.03}$
Fe complex gauss. line sigma (keV)	0.25 (frozen)	0.25 (frozen)
Fe complex gauss. line norm.	$0.0180^{+0.0006}_{-0.0009}$	$0.027^{+0.001}_{-0.001}$
Bknpower index 1	$0.76^{+0.15}_{-0.10}$	$1.48^{+0.40}_{-0.94}$
Bknpower break (keV)	$5.74^{+0.17}_{-0.09}$	$5.60^{+0.22}_{-0.08}$
Bknpower index 2	$2.9^{+0.3}_{-0.2}$	$3.5^{+0.3}_{-0.2}$
Bknpower norm.	$0.15^{+0.03}_{-0.02}$	$1.27^{+1.36}_{-0.09}$
Bknpower PD (%)	$24.9^{+0.7}_{-0.6}$	$11.8^{+0.5}_{-0.5}$
Bknpower PA (deg)	$90.7^{+0.6}_{-0.6}$	$92.4^{+0.9}_{-1.0}$
Diskbb $T_{\rm in}$ (keV)	$0.37^{+0.06}_{-0.08}$	$0.27^{+0.04}_{-0.04}$
Diskbb norm. (10^4)	4^{+5}_{-4}	5^{+7}_{-3}
Diskbb PD (%)	5^{+1}_{-3}	undefined
Diskbb PA (deg)	undefined	undefined
Gauss. line 1 energy (keV)	2.07 (frozen)	2.07 (frozen)
Gauss. line 1 sigma (keV)	0.15 (frozen)	0.15 (frozen)
Gauss. line 1 norm.	$-0.12^{+0.04}_{-0.02}$	$-0.092^{+0.009}_{-0.156}$
Gauss. line 2 energy (keV)	2.4 (frozen)	2.4 (frozen)
Gauss. line 2 sigma (keV)	0.15 (frozen)	0.15 (frozen)
Gauss. line 2 norm.	$-0.014^{+0.009}_{-0.006}$	0.0 (frozen)
Gauss. line 3 energy (keV)	2.8 (frozen)	2.8 (frozen)
Gauss. line 3 sigma (keV)	0.15 (frozen)	0.15 (frozen)
Gauss. line 3 norm.	$-0.015^{+0.006}_{-0.003}$	$-0.016^{+0.002}_{-0.008}$
Gauss. line 4 energy (keV)	3.95 (frozen)	3.95 (frozen)
Gauss. line 4 sigma (keV)	0.15 (frozen)	0.15 (frozen)
Gauss. line 4 norm.	$0.0021^{+0.0006}_{-0.0007}$	$0.0035^{+0.0008}_{-0.0017}$
IXPE/det1 MPL γ	0.0 (frozen)	0.0 (frozen)
IXPE/det1 MPL f	1.0 (frozen)	1.0 (frozen)
IXPE/det2 MPL γ	0.029 ± 0.008	-0.008 ± 0.007
IXPE/det2 MPL f	0.998 ± 0.010	0.955 ± 0.009
IXPE/det3 MPL γ	-0.016 ± 0.008	-0.011 ± 0.007
IXPE/det3 MPL f	0.904 ± 0.009	0.911 ± 0.008
χ^2/d.o.f.	800.6/718	810.2/719
Null probability (%)	1.7	1.0

with non-thermal Comptonization produced by a steep electron distribution and models with the dominance of reflection component, in the geometry where the reflector partially covers the primary X-ray source. The diversity of alternatives prevented firm conclusions on the observed luminosity in this state, always found to be of the order of 10^{38} erg s^{-1}, but precise numbers varying by a factor of 4–5, depending on the model. At the same time, the uncertainty on the mass of the compact object [18, 23, 40–42], along with its nature, a neutron
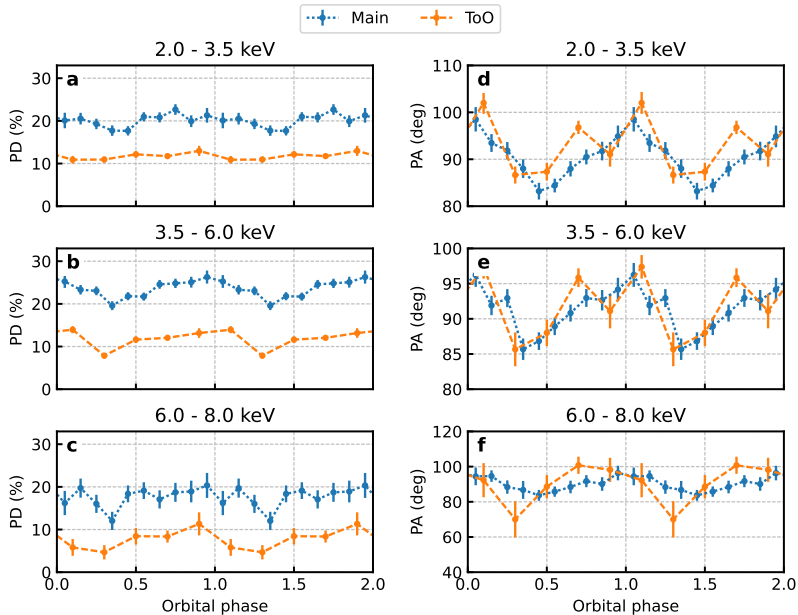
Fig. A2 Orbital phase dependence of polarization. The PD **(a)**–**(c)** and PA **(d)**–**(f)** in different energy bands (2–3.5 keV, **a, d**; 3.5–6 keV, **b, e**; 6–8 keV, **c, f**) for the Main (in blue) and ToO (in orange) observations are shown.

star or a black hole, as well as the chemical composition of the hydrogen-poor matter dragged from the WR companion make the estimates of the Eddington luminosity likewise uncertain. It has therefore been unclear what kind of accretion regime to expect in this state.

The source occasionally displays spectral transitions to the soft state, accompanied by the increase of the soft X-ray luminosity and suppression of the radio emission. Changes of spectral shape have been attributed to the changes of the accretion-ejection geometry. The X-ray spectra of soft and ultra-soft states resemble thermal emission of the multicolour accretion disc [29], typically seen at luminosities between the Eddington limit and down to 10% of that. After the transition, the major radio flare may happen, when the highest radio fluxes among all X-ray binaries can be reached [43, 44]. The second IXPE run was triggered as a target of opportunity observation following the increase of the soft X-ray and drop of the radio fluxes, when the source transited to the suppressed radio state. IXPE caught the source after the radio recovered, in its intermediate X-ray state, during the minor flaring radio episodes (Fig. A4 and [24]).

On shorter timescales, prominent orbital variability of X-ray, γ-ray, IR and radio fluxes [23, 45–48], as well as X-ray and IR line shapes [17–19, 49] has been observed. Our multiwavelength observations show orbital flux variations in all bands (Figs. A8–A10). This variability is related to the movement of
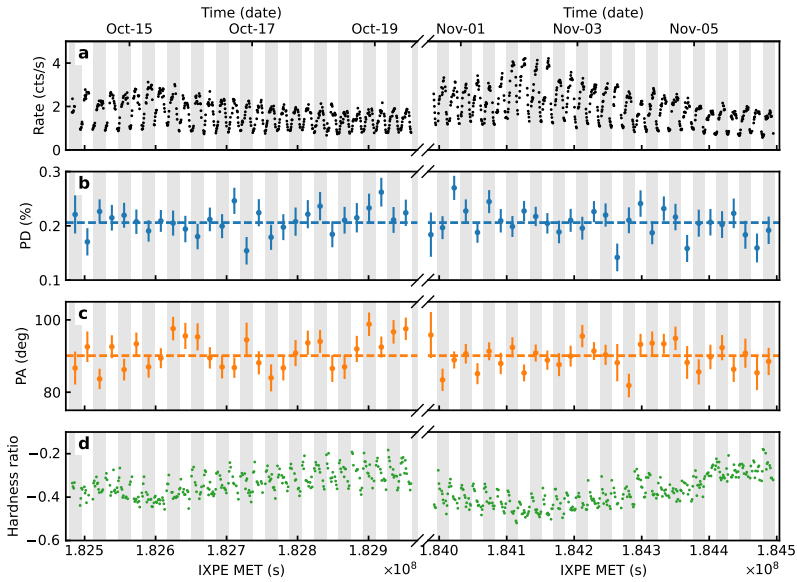
Fig. A3 Variation with time of flux and polarization for the IXPE Main observation. **(a)** The total rate in the 2–8 keV energy range, binned in time intervals of 500 s. The PD **(b)** and the PA **(c)** are averaged over one orbit, as defined by the ephemeris of [21]. Dashed horizontal lines are the average values. **(d)** The hardness ratio defined as the ratio of the difference in the IXPE count rates in the 4–8 and 2–4 keV energy bands to their sum in 1000 s time bins. Alternating vertical bands identify different orbits.
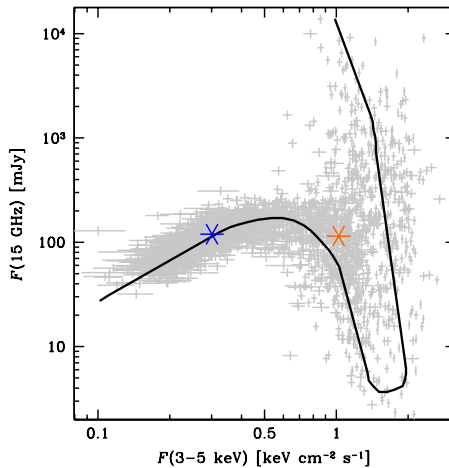
Fig. A4 Radio-X-ray evolution track from historical radio and X-ray observations. Blue and orange stars indicate the fluxes during the Main and ToO observations, respectively.
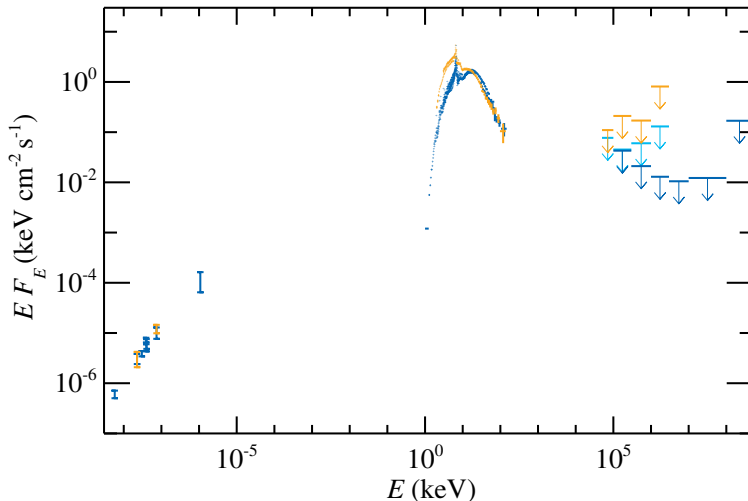
Fig. A5 Broadband spectral energy distribution of Cyg X-3. The SED for the Main (blue) and ToO (orange) observations are from the facilities described in the text.

the compact object in an orbit with the companion star and varying absorption along the line of sight. X-ray orbital profiles are asymmetric, indicating presence of several absorbing components [23, 50], hence, maximal absorption phase (phase of the minimal X-ray flux) does not necessarily coincide with the phase of superior conjunction (compact object behind the WR star). Recent study suggest that these phases are close, though, $\phi_{sc} = -0.066 \pm 0.006$ [23]. In Fig. A6 we show the evolution of the lower-energy spectra observed with NICER throughout the orbital phases during the October-November multiwavelength campaign. Interestingly, we find that changes of spectra as a function of orbital phase do not follow simple pattern of changing absorption, as in this case the spectral shape is expected to change substantially. Instead, we mostly see variations of spectral normalisation, which are more in line with changing of the characteristic reflection angle [51].

At all phases, the energies 6–8 keV are dominated by the complex of the iron emission lines (Fe K lines). It consists of the neutral iron, iron XXV and XXVI [18, 19, 42]. Behaviour of these lines with the orbital phase varies, allowing to relate the hydrogen-like iron with the compact object [18]. Analysis of the ratios of the forbidden, resonance and intercombination lines indicates that these species are located in a dense medium, which nevertheless has high ionization [19]. Interestingly, the Chandra/HETGS spectrum of Cyg X-3 is so far the only fully resolved Fe K complex in an astrophysical source [42].

We performed broadband spectral modelling, for both Main and ToO runs, using the data from NuSTAR and SRG/ART-XC instruments. We acknowledge a complexity of such modelling in light of the high-amplitude orbital variability. The small statistical errors of spectra cause the average spectra to be non-representative, as the orbital variations of flux and hardness alter
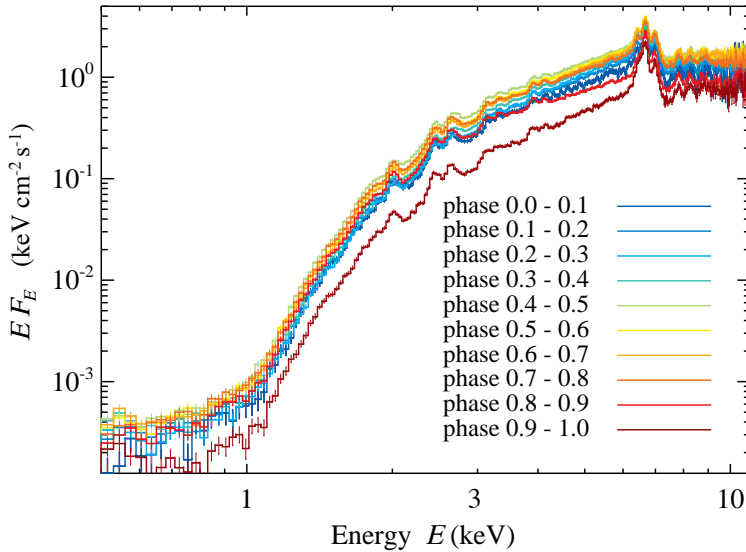
Fig. A6 X-ray SED of Cyg X-3 from NICER. Orbital phase-folded X-ray spectra are taken during November observations with NICER.

the average spectral shape. For this reason we add 1% systematic errors to the data. While for the Main observation, we find that a good fit can be obtained when summing up all spectra (i.e. the spectral shape does not evolve substantially with the orbital phase), for the ToO observation we found that we may only use spectra averaged over orbital phases 0.25–0.75, i.e. close to the inferior, when the intrabinary absorption is smallest. Motivated by the polarization properties, we consider the model where the 2–8 keV spectrum is dominated by the reflection component. We fit the data with the model REFLECT×SMEDGE×(DISKPBB+NTHCOMP)+GAUSSIAN+GAUSSIAN and set the parameter rel_refl= −1, which means that we do not take the contribution of the incident X-ray emission into account in the resulting spectra. For the Main observation, we find that only one gaussian is capable to describe the line around 6.5 keV and the thermal component in the incident spectrum is not needed, so we set its normalization to zero. We get a good fit with χ^2/d.o.f. = 1.05, see Fig. A7 and Table A2.

Physically, the model describes the reflection spectrum of the neutral matter, that is produced by the continuum composed of the multicolour accretion disc and a soft Comptonization continuum, which are similar to the soft spectra observed from the ULXs [1]. The transition from the hard (radio-quiescent) to the intermediate (minor flaring) state in this model is related to the changing shape of the intrinsic continuum, which we nevertheless do not see directly, but only via its reflection. In order to describe the spectra of the ToO observation, we need two lines around ∼ 6.5 keV and a softer incident X-ray spectrum, whose shape we model as sum of the thermal component described by the multicolour disc and the soft power-law-like Comptonization continuum. We

Table A2 Model parameters for the NuSTAR fit. The model reads: REFLECT×SMEDGE×(DISKPBB + NTHCOMP) + GAUSSIAN + GAUSSIAN. In the Main observation, two components have not been used (a gaussian around 6.4 keV and an intrinsic multicolour disc component).

	Main	ToO
reflect rel_refl	−1 (frozen)	−1 (frozen)
reflect Redshift	0 (frozen)	0 (frozen)
reflect abund	1 (frozen)	1 (frozen)
reflect Fe_{abund}	0.76 ± 0.03	0.43 ± 0.02
reflect cosIncl	0.26 ± 0.06	$0.05^{+0.002}_{-0.05}$
smedge edgeE (keV)	8.70 ± 0.05	8.79 ± 0.03
smedge MaxTau	0.42 ± 0.04	0.39 ± 0.03
smedge index	−2.67 (frozen)	−2.67 (frozen)
smedge width	$1.3^{+0.3}_{-0.2}$	0.59 ± 0.08
diskpbb kT_{in} (keV)	−	0.99 ± 0.02
diskpbb p	−	$0.50^{+0.03}_{-0.5}$
diskpbb norm (10^4)	−	$1.24^{+0.34}_{-0.14}$
nthcomp Γ	2.70 ± 0.04	$3.10^{+0.02}_{-0.04}$
nthcomp kT_e (keV)	51^{+31}_{-13}	51 (frozen)
nthcomp kT_{bb} (keV)	0.63 ± 0.02	$= kT_{in}$
nthcomp inp_type 0/1	0 (frozen)	0 (frozen)
nthcomp Redshift	0 (frozen)	0 (frozen)
nthcomp norm	3.4 ± 0.5	5.4 ± 2.7
gaussian LineE (keV)	6.524 ± 0.004	6.61 ± 0.03
gaussian Sigma (keV)	0.212 ± 0.007	0.13 ± 0.02
gaussian norm. (10^{-2})	1.09 ± 0.03	0.88 ± 0.15
gaussian LineE (keV)	−	6.41 (frozen)
gaussian Sigma (keV)	−	0.28 ± 0.06
gaussian norm. (10^{-2})	−	1.0 ± 0.2
χ^2/d.o.f.	1038/989	920/884

get a good fit with χ^2/d.o.f. = 1.04. We find that the spectra can also be fit with other models, including those where the primary X-ray emission and reflection both substantially contribute to the X-ray continuum, repeating the diversity of models presented in [26], and confirm that the polarimetric information is vital to choose from variety of options. Finally, we note that no currently available public model can account for the complex properties of the reflection in the proposed scenario: we need a convolution model, as we use complex incident spectrum, that considers a hydrogen-poor material and can self-consistently account for the lines.

A.2.1 X-rays and gamma-rays

Cotemporaneous observations of Cyg X-3 during the Main run have been performed with NICER. NICER is a soft X-ray instrument onboard the International Space Station (ISS), launched in June 2017. It consists of 56 co-aligned concentrator X-ray optics, each of which is paired with a single silicon drift detector. It is non-imaging, but offers large collecting area, and provides unmatched time resolution in the soft X-ray bandpass, and sensitive across 0.2–12 keV. NICER provided monitoring during the IXPE campaign,
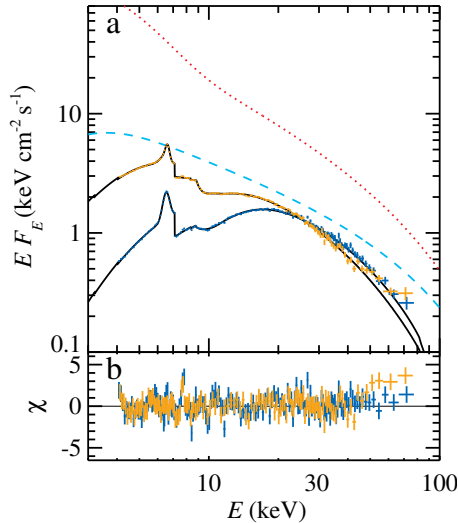
Fig. A7 Modelled broadband X-ray SED. (a) Spectral models of reflection-dominated spectra during Main and ToO observations (black solid lines), NuSTAR data from the Main observation (blue crosses) and ToO observation (orange crosses) and the corresponding intrinsic X-ray continua: Main (cyan dashed line) and ToO (red dotted line) needed to produce the observed reflection spectra. **(b)** The residuals of the models relative to the data in units of the errors.

Table A3 Summary of cotemporaneous X-ray and γ-ray observations.

Facility	Energy (keV)	MJD−59800	Average flux (keV cm^{-2} s^{-1})
IXPE	2–8	66–71, 83–89	0.96
		138–142	2.6
NICER	0.5–12	84–87	1.6
ART-XC	4–30	87	2.9
INTEGRAL	20–100	84–88	1.1
		138	0.9
NuSTAR	3–50	65–66	3.5
		138–139	6.0
AGILE	$10^5 - 5 \times 10^7$	66–71, 83–89	< 0.033
		138–142	< 0.22
Fermi	$10^5 - 10^8$	62–73	$\lesssim 0.01$

observing Cyg X-3 between MJD 59884 and 59887. The resulting average and orbital-phase resolved spectra are shown in Figs. A5 and A6. NICER has good capabilities for timing studies. We checked for the presence of the short-term (of the order of seconds) variability, but did not find any significant intrinsic fluctuations above the noise level. This is in line with previous findings [52].

Broadband X-ray spectral coverage of Cyg X-3 during the Main and ToO runs were performed with the Nuclear Spectroscopic Telescope Array (NuS-TAR) observatory. NuSTAR consists of two identical X-ray telescope modules,
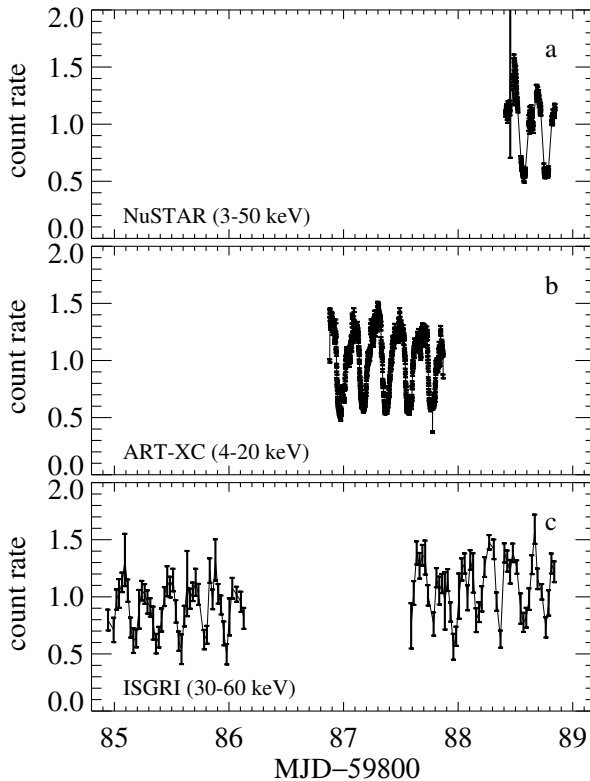
Fig. A8 X-ray light curves of Cyg X-3. X-ray count rates normalized to the average during the Main observation obtained by three X-ray telescopes: NuSTAR, SRG/ART-XC and INTEGRAL/ISGRI.

referred to as FPMA and FPMB [53]. It provides X-ray imaging, spectroscopy and timing in the energy range of 3–79 keV with an angular resolution of 18 arcsec (FWHM) and spectral resolution of 400 eV (FWHM) at 10 keV. We use two NuSTAR datasets: the first one was carried out on 5 November 2022 (ObsIDs: 90802323004) with the on-source exposure of ∼ 16 ks (during Main observation) and the second one performed on 25 December 2022 (ObsIDs: 90801336002) with ∼ 36 ks exposure (during ToO observation). Both observations covered several orbital cycles of the system, which allowed to perform phase-resolved spectroscopy. The NuSTAR data were processed with the standard NuSTAR Data Analysis Software (nustardas 4May21 v2.1.1) provided under heasoft v6.29 with the caldb version 20201217. Circular 100 arcsec radius regions were used for both source and background spectra extraction. The source region was centered on the locations of Cyg X-3 and the background region was selected from a sourceless region in the detector image. All obtained spectra were grouped to have at least 25 counts per bin using the grppha tool. The final data analysis (timing and spectral) was performed with the heasoft 6.29 software package.

The Mikhail Pavlinsky ART-XC telescope carried out one observation of Cyg X-3 on 4 November 2022 (MJD 59887) simultaneously with IXPE, with the 86 ks net exposure. ART-XC is a grazing incidence focusing X-ray telescope on board the Spectrum-Rontgen-Gamma observatory (SRG, [54]). The telescope includes seven independent modules and provides imaging, timing and spectroscopy in the 4–30 keV energy range with the total effective area of ~ 450 cm^2 at 6 keV, angular resolution of 45 arcsec, energy resolution of 1.4 keV at 6 keV and timing resolution of $23\mu s$ [55]. ART-XC data were processed with the analysis software ARTPRODUCTSv1.0 and the CALDB (calibration data base) version 20220908. The ART-XC observation was performed approximately one day before the first NuSTAR observation (Main), therefore spectral parameters measured by ART-XC are close to the ones determined from NuSTAR data (see Table A2) with the flux of $\sim 4.6 \times 10^{-9}$ erg cm^{-2} s^{-1} in the 4–30 keV energy band.

INTEGRAL observed Cyg X-3 simultaneously with IXPE two times: the first observation lasted from 2022-11-01 21:11 to 2022-11-05 20:23 UT; the second observation lasted from 2022–12-25 02:37 to 2022-12-25 14:53 UT. Our data analysis is focused on ISGRI, the low energy part of the IBIS telescope [56, 57]. The INTEGRAL data were reduced using the latest release of the standard On-line Scientific Analysis (OSA, version 11.2), distributed by the INTEGRAL Science Data Centre (ISDC, [58]) through the multi-messenger online data analysis platform (MMODA, [59]). The ISGRI spectra were extracted in the range 30–150 keV with a response matrix with 16 standard channels. The spectra of the first and the second observations were fitted with a simple power law with photon index of 3.6±0.1 and 3.4±0.1, respectively. The fluxes in the range 20–100 keV are 1.7×10^{-9} and 1.4×10^{-9} erg cm^{-2} s^{-1}, respectively.

The Fermi/LAT data on Cyg X-3 was collected during MJD 59862–59873 in 0.1–500 GeV energy band. Fermi is located at a low-Earth orbit with 90 min period and normally operates in survey mode, which allows the instrument to cover the whole sky in approximately 3 h (see full details of the instrumentation in [6]). The standard binned likelihood analysis [60] was performed with the latest available `Fermitools v.2.0.8` software. The analysis was carried out using the latest Pass 8 reprocessed data (P8R3) [61] for the SOURCE event class (maximum zenith angle 90°) taken at the region centred at Cyg X-3 coordinates. The analysis is based on fitting of the spatial/spectral model the the 14°-radius region around the source. The model of the region included all sources from the 4FGL DR3 catalogue [62], as well as components for isotropic and galactic diffuse emissions given by the standard spatial and spectral templates `iso_P8R3_SOURCE_V3_v1.txt` and `gll_iem_v07.fits`.

The spectral template for each 4FGL source present in the model was selected according to the catalogue. The normalisations of the spectra of all sources, as well as the normalisations of the Galactic diffuse and isotropic backgrounds, were assumed to be free parameters during the fit. We note also that Cyg X-3 is present in 4FGL catalogue as 4FGL J2032.6+4053 point-like source with the log-parabola-type spectrum. Following the recommendation of

the Fermi-LAT collaboration, we performed the analysis with enabled energy dispersion handling. To minimise the potential effects from the sources present beyond the considered region of interest, we additionally included into the model all the 4FGL sources up to 10° beyond this radius, with all the spectral parameters fixed to the catalogue values. The results of the described analysis performed in relatively narrow energy bins are shown in Fig. A5. The source was not detected in any of the selected energy bins with the higher than 2σ significance (test-statistic 4.0). The shown upper limits correspond to 95% false-chance probability and were calculated with the help of `IntegralUpperLimit` python module, provided within `Fermitools`.

Cyg X-3 was also observed in the γ-rays with Astrorivelatore Gamma ad Immagini LEggero (AGILE). AGILE satellite [63] is a space mission of the Italian Space Agency (ASI) devoted to X-ray and γ-ray astrophysics, operating since 2007 in a low Earth equatorial orbit. AGILE in its spinning observation mode performs a monitoring of about 80% of the entire sky with its imaging detectors every 7 mins. The data collected with the γ-ray imager (GRID, 30 MeV–50 GeV), has been analysed over the periods of MJD 59866–59871, 59883–59889 (Main) and MJD 59938–59942. The data analysis was carried out using the last available AGILE-GRID software package (Build 25), `FM3.119` calibrated filter, `H0025` response matrices, and consolidated archive (`ASDCSTDk`) from the AGILE Data Center at SSDC [64]. We applied South Atlantic Anomaly event cuts and 80° Earth albedo filtering, by taking into account only incoming gamma-ray events with an off-axis angle lower than 60°. Flux determination was calculated using the AGILE multi-source likelihood analysis (MSLA) software [65] based on the Test Statistic (TS) method [60]. We performed the MSLA for Cyg X-3 by including, as background sources, the 3 nearby pulsars of the Cygnus region (PSR J2021+3651, PSR J2021+4026 and PSR J2032+4127), which are known to be persistent and intense γ-ray emitters, located at angular distances smaller than 5° from the source. For the background sources, we assumed the long-term integration spectra, as reported in the 2AGL Catalog [66]. We modeled the γ-ray spectrum for Cyg X-3 with a simple power law with a standard 2.0 photon index. The source was in the quiescent and intermediate state during the time of IXPE observations, hence no prominent γ-ray activity has been detected. The full-band AGILE-GRID upper limits are given in Table A3 and are consistent with the Fermi/LAT limits. Spectral ULs (50 MeV–3 GeV) are shown in Fig. A5.

A.2.2 Radio and submillimeter

Monitoring of Cyg X-3 at radio wavelengths cotemporaneous with IXPE was performed using Large Array of the Arcminute MicroKelvin Imager (AMI-LA), RATAN-600, Medicina, Effelsberg, upgraded Giant Metrewave Radio Telescope (uGMRT) and Submillimeter Array (SMA) telescopes. This coverage allowed to identify the state of the source, produce the broadband spectrum and make constraints on the PA at longer wavelengths. Summary of these observations can be found in Table A4 and in Figs. A9 and A10.
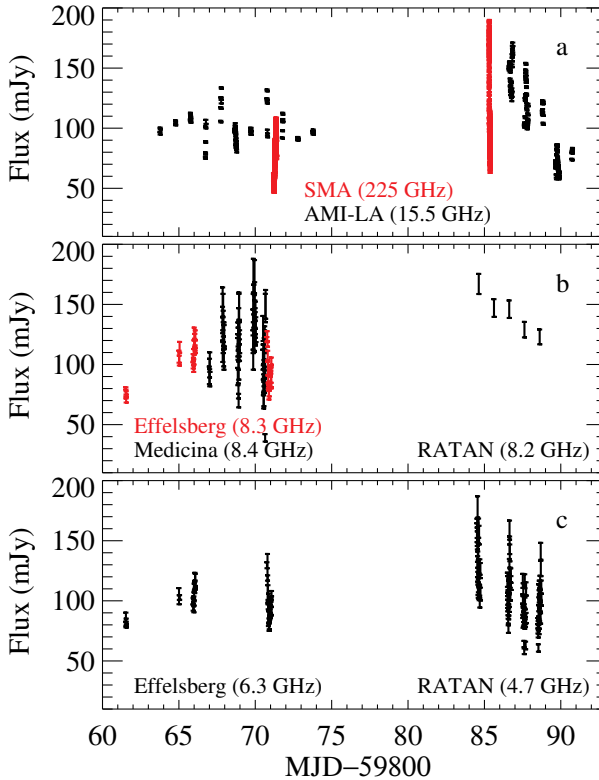
Fig. A9 Radio and sub-mm light curves of Cyg X-3. The light curves of the source around the dates of Main observation as obtained with various telescopes. Note high intraday variations of the radio flux caused by the orbital variability.

Cyg X-3 was observed at 15.5 GHz with the AMI-LA [67, 68] during the IXPE observing campaigns. The AMI-LA consists of eight 13-m antennas, which measure one polarization (Stokes $I+Q$), over a wide bandwidth of 12 to 18 GHz in 8 broad channels. The observations were usually $\sim$ 1-hr long, with some longer observations, up to $\sim$ 6 hr, from Nov 3rd to 6th. Each observation consisted of 10-min scans on Cyg X-3, interleaved with short observations of a nearby compact calibrator source J2052+3635, which was used to apply phase corrections, and monitor the sensitivity of the telescope. The data were processed using standard procedures: (i) to automatically eliminate bad data due to various technical problems and interference; (ii) manually edit remaining interference (which included the end channels, which were more prone to interference), and periods of heavy rain; (iii) use the interleaved observations of J2052+3635 provided the initial phase calibration of each antenna in the array throughout each observation, (iv) set the overall flux density scale by comparison with daily observations of the standard calibrator source 3C 286, together with the "rain gauge" measurements made during the observations to correct for varying atmospheric conditions [67]. Flux densities at 15.5 GHz

Table A4 Summary of radio and sub-millimeter observations. IXPE observations were performed on MJD 59866–59871, 59883–59889 and 59938–59942.

Telescope	Date MJD−59800	Frequency (GHz)	Average flux (mJy)	Variance (mJy)	PD %	PA (deg)
SMA	71	225	76	36	2.84 ± 1.14	−28 ± 11.5
	85	225	86	35	2.21 ± 0.44	−6.0 ± 5.8
AMI-LA	63–90	15.5	106	27		
	137–139	15.5	126	24		
Medicina	66–70	8.4	118	26		
Effelsberg	61–70	8.3	99	16		
Effelsberg	61–70	6.3	99	12		
RATAN	84–88	8.2	142	15		
		4.7	106	24		
	138	4.7	107	36		
uGMRT	85–86	1.2	81	14		

were derived for 10-min averages, from the central 6 broad frequency channels (i.e. covering 13.6−17.4 GHz). The resulting light-curves are shown in Fig. A9a.

To monitor Cyg X-3 we triggered a Target-of-Opportunity program with the 32-m Medicina radio telescope in order to follow the evolution of the radio emission during the IXPE observations. We carried out observations at the central frequency of 8.4 GHz (X-band) with the Total Power continuum back-end on 14–18 October 2022. Each session lasted 5 h per day in order to track the fast flux density variations even during the quiescent state. We performed On-The-Fly cross-scans and maps along the Right Ascension and Declination directions, setting a bandwidth of 230 MHz to avoid the strongest radio frequency interference (RFI). Scans were performed along a length of 0.7° at a velocity of 2.4°/min at 8.4 GHz, with a sampling time of 40 ms. Data were calibrated through repeated cross-scans centered on NGC 7027 at different elevations. This calibrator has the advantage to be very close in elevation to the target. We extrapolated the calibrator flux density according to [69]. The calibration procedure included the corrections for the frequency-dependent gain curves, in addition to the compensations for the pointing offset measured on each scan. The data analysis was performed with the Single-Dish-Imager, a software designed to perform automated baseline subtraction, radio interference rejection and calibration [70]. We estimate the final accuracy of our measurements to be ∼ 8% at 8.4 GHz. The resulting light curve is presented in Fig. A9b.

Observations of Cyg X-3 were performed with the 100-m Effelsberg dish on 2022 Oct 9, 13, 14, and 18 with the S45mm-receiver and the spectropolarimeter backend. Acquisitions were performed over two bands, 5.4–7.2 (f_{center} = 6.3 GHz) and in two subbands of the second band 7.6–8.2 & 8.4–9.0 GHz (f_{center} = 8.3 GHz). These frequency ranges (especially the omission of the center part of the second band) were chosen to avoid RFI. We measured the flux density with the cross-scans-method, doing several subscans in
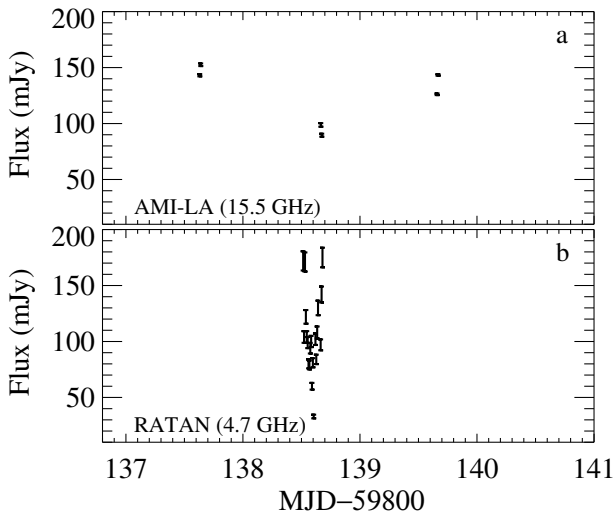
Fig. A10 Radio light curves during the ToO observation. Orbital variability is clearly present, but the average fluxes are slightly higher as compared to the Main observation.

azimuth and elevation (12 in the case of Cyg X-3). All subscans were corrected for pointing offsets and averaged. After that the atmospheric absorption and the loss of sensitivity due to gravitational deformation of the dish were corrected (both effects are rather small). The final calibration was done via suitable flux density calibrators (i.e. 3C 286 and NGC 7027). For the polarization, instrumental effects were corrected by a Müller matrix method. A number of calibrators were observed before and after the actual observations of Cyg X-3, to determine the various effects properly. No polarization was detected in the Effelsberg data meaning that the level of polarization must be lower than 5%. The resulting light-curves are shown in Fig A9b and c.

Cyg X-3 was monitored at 4.7 and 8.2 GHz on a daily basis at the North sector of RATAN-600 telescope using the uncooled tuned receiver in the total power radiometer mode [71]. This mode allows to perform sensitive observations, with precision being limited by the presence of an RFI. Typical accuracy of 5% for fluxes near 100 mJy has been reached during the cotemporaneous observations with IXPE. The main parameters of the antenna (effective area and beam size) were calibrated with the source NGC 7027. Observations of NGC 7027 have in the multi-azimuthal mode gave flux density of 5.38 Jy at 4.7 GHz, in agreement with the standards [69]. Additional intraday observations of Cyg X-3 at 4.7 and 8.2 GHz were carried out with the "Southern sector and Flat mirror" configuration. The increased field of view (±30°, as compared to the observations with the North Sector) in this configuration allowed to follow the source longer. For discrete antenna configurations (with step 2°) we carried out 31 measurements, taken every 10 minutes. The resulting light-curves

at 4.7 and 8.2 GHz are shown in Fig. A9b and c for the Main run, and in Fig. A10b for the ToO run.

Observations of Cyg X-3 during the Main IXPE observation with uGMRT were performed following the Director's Discretionary Time (DDT) requested. Due to scheduling constraints, the observations were only granted on 2 and 3 November for ∼ 5 h each, i.e. a full orbit. Observations were performed at Band 5 (1–1.4 GHz) using a correlation bandwidth of 400 MHz and 2048 frequency channels. The observing strategy featured cross-scans on the source interleaved with calibrators for phasing and flux references. The absolute flux density scale is tied to the Perley-Butler 2017 scale. The CAPTURE pipeline [72] was used to analyse the GMRT data. The error on the total flux density of the source includes the error on the Gaussian fit and the absolute flux density error of 10% added in quadrature.

Cygnus X-3 was observed by the SMA located on Maunakea in Hawaii on 19 October 2022 and 2 November 2022. The SMA observations use two orthogonally polarized receivers, tuned to the same frequency range in the full polarization mode. These receivers are inherently linearly polarized but are converted to circular using the quarter-wave plates of the SMA polarimeter [73]. The lower sideband (LSB) and upper sideband (USB) covered 209–221 and 229–241 GHz, respectively. Each sideband was divided into six chunks, with a bandwidth of 2 GHz, and a fixed channel width of 140 kHz. The SMA data were calibrated with the MIR software package. Instrumental polarization was calibrated independently for USB and LSB and removed from the data. The polarized intensity, PA and PD were derived from the Stokes I, Q, and U visibilities. MWC 349 A and BL Lac were used for both flux and polarization calibration and Neptune was used for flux calibration. Observations on 19 October were done with four antennas and a median 225 GHz opacity of ∼0.2 while those on 2 November were obtained with seven antennas and a median opacity of ∼0.1. Due to the low level of polarization the overall polarization measurements are of low statistical significance, especially for the 19 October observation. For the 19 October observation it was necessary to exclude 1 of the four antenna and in the Nov. 2nd observation data after UT 9.2 was excluded due to significant increase in phase instability as a result of weather conditions. The overall flux uncertainty in an absolute sense is ∼5% of the continuum flux value. The values shown in Table A4 are averages over the entire observation of that day. Light curves of the total intensity (Stokes I) for the two days are shown in Fig A9a.

A.3 Modelling

A.3.1 Analytical modelling of the funnel

At high accretion rates, the accretion disc possesses a critical point, the spherization radius, at which the matter can leave the disc pushed by radiation pressure forces [29, 30]. It forms an axially symmetric outflow with an empty funnel around the disc axis. Radiation emitted by the accretion disc cannot
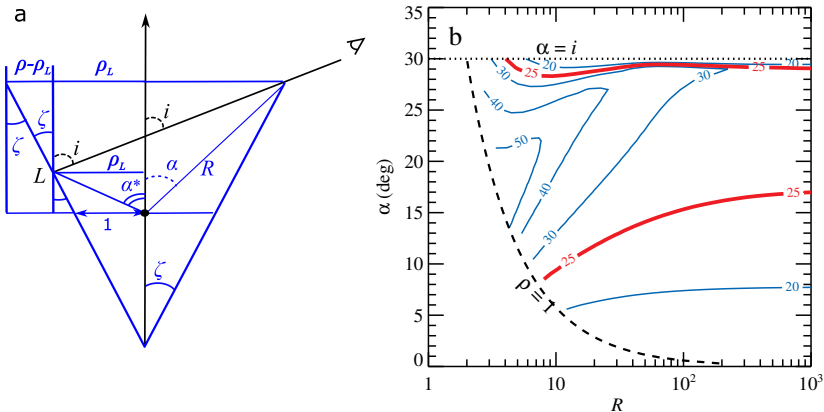
Fig. A11 Detailed geometry of the reflecting funnel and its polarimetric characteristics. (a) Geometry of the funnel is shown with L being the lowest visible point for the given inclination i, and the angle α^* is its colatitude. **(b)** The contour plots of constant PD (in %) for the fixed observer inclination ($i = 30°$), as function of the model parameters (α, R). The region above $\alpha = i$ is not allowed because the central source would be visible. The region below $\rho = 1$ curve (i.e. $R = 1/\sin\alpha$) corresponds to a wind converging towards the axis, which is not possible. Red contours show the allowed model parameters.

escape freely, but is collimated by the funnel walls. As a result an observer looking along the funnel will see strongly amplified emission. On the other hand, an observer located at a large inclination angle to the axis sees the photosphere that is situated at a significant distance from the central source, which depends on the mass loss rate that in turn depends on the accretion rate. Such an observer can see radiation scattered and reflected from the funnel walls at high elevations, where the matter is mostly neutral.

We approximate the funnel geometry by the truncated cone (see Fig. 3a), which has two main parameters: R, the distance to the X-ray photosphere, where the optical depth becomes comparable to unity, scaled to the inner radius of the outflow in the accretion disc plane, and the angle α at which the upper boundary of the funnel is seen from the primary X-ray source. Unpolarized radiation emitted by the central source (which is the inner accretion disc and the collimated radiation from the inner part of the funnel) is impinging on the wall higher up in the funnel. The probability for photons to be reflected is proportional to the energy-dependent single-scattering albedo λ_E, which is the ratio of the scattering opacity to the total (scattering and photo-electric) opacity. Because in the IXPE range $\lambda_E \ll 1$, the reflected radiation is dominated by single-scattered photons. This radiation is polarized with the PD for Thomson scattering (valid in the IXPE range) being dependent on the cosine of the scattering angle μ as

$$P(\mu) = \frac{1 - \mu^2}{1 + \mu^2}. \tag{A1}$$

The PA of this radiation, which we denote as χ_0, lies perpendicular to the scattering plane. The intensity of reflected radiation is proportional to the phase function $\frac{3}{4}(1+\mu^2)$ and the ratio $\eta_0/(\eta+\eta_0)$ (page 146 in [74]), where η_0 is the cosine of the angle between the local normal to the funnel wall and the incoming radiation beam, while η is the cosine of the angle between direction to the observer and the normal. Thus the Stokes parameters of the reflected radiation are

$$
\begin{pmatrix} I_E \\ Q_E \\ U_E \\ 0 \end{pmatrix} = \lambda_E \frac{3}{4}(1+\mu^2)\frac{L_E}{4\pi r^2} \begin{pmatrix} 1 \\ P\cos 2\chi_0 \\ P\sin 2\chi_0 \end{pmatrix} \frac{\eta_0}{\eta+\eta_0},
\tag{A2}
$$

where L_E is the luminosity of the central object and r is the distance from the centre to the element of the funnel. Integrating this expression over the visible surface of the funnel, we get the observed flux and the corresponding Stokes parameters. We see that all Stokes parameters in the single-scattering approximation are proportional to λ_E and therefore the PD of the total radiation is energy-independent.

A natural condition for the primary source to be obscured is $i > \alpha$. In Fig. 3b we show the contours of constant PD as a functions of α and i, for a chosen $R = 10$. Two branches of solutions are possible for $i \lesssim 40°$: the lower branch with a narrow funnel $\alpha \sim 10°$, and upper branch with $\alpha \approx i$, where the observer looks almost along the funnel walls. We note tightly-packed contours near this branch, indicating that any small, a few degrees, variations of the opening angle would cause changes in the observed PD by tens of per cent. In contrast, the time dependence of the observed PD, averaged over orbital phase, is consistent with constant, with the standard deviation of 2.5% (see Fig. A3).

In Fig. A11b we show the dependence of PD parameters α and R, for the fixed $i = 30°$. We see the same two branches of a possible solution corresponding to PD=25% and consider only the lower one for the aforementioned reason. The part of the diagram below $R = 1/\sin\alpha$ is forbidden, because it corresponds to $\rho < 1$, i.e. a converging towards the axis outflow. For the observed PD, the minimum possible size of the photosphere is $R = 8$, which corresponds to $\alpha = 8°$. At a larger R, the required α increases, saturating at $\approx 17°$.

The computed PDs in Figs. 3b and A11b correspond to the case when polarization is produced solely at the inner surface of the funnel, which can be realised for a very high Thomson optical depth. These conditions can be applicable to the Main observation. Changes of polarization properties in the ToO observation can be caused by the reduction of the Thomson optical depth of the funnel. In this case, we expect to see scattered radiation from some volume around the funnel walls, rather than solely from its inner surface. This leads to the increased role of photons scattered at small angles, hence reduction of the net polarization. Alternatively, the scattering may proceed right above the funnel, in the optically thin WR wind. Our estimates of the Thomson

optical depth from the mass loss rate and wind velocity, assuming hydrogen-poor material [23] give $\tau_{\mathrm{T,WR}} \sim 0.1-0.5$. For small optical depth, $\tau_{\mathrm{T,WR}} \approx 0.1$, the spectrum of the scattered radiation closely resembles that of the incident continuum. However, the observed spectral shapes do not correspond to the spectra of any other accreting source. For larger $\tau_{\mathrm{T,WR}} \sim 1$, on the other hand, the effect of multiple scattering tends to decrease the PD at higher energies within IXPE range, which is not observed. Thus, to be consistent with the data, this scenario requires tight constraints $\tau_{\mathrm{T,WR}} \approx 0.3-0.5$, which might be hard to realise. Our calculations show that the resulting PD in this scenario is nearly independent of the funnel angle α at any inclination $i > \alpha$, hence this case cannot account for the change of PD between Main and ToO observations. If we consider this scenario for the ToO observation, then the observed PD$\approx 12°$ translates to the inclination $i \approx 27°$ according to Eq. (A1).

An important property of the observed X-ray polarization is its prominent orbital phase-dependent variations (Fig. 2). Interestingly, the polarization is mostly "misaligned" from the East-West direction (i.e., from the orbital plane) during the phases of inferior and superior conjunctions, when the left-right directions (that give non-zero contributions to the Stokes U) are expected to be symmetric in the simple picture with the cone-shaped funnel pointing in the direction of the orbital axis. In the proposed scenario, the outflow from the compact object is expected to collide with the wind of the WR star, resulting in an asymmetry of the funnel and its surrounding.

We first considered geometries where the funnel is shaped as an oblique, truncated cone and also modelled a situation where the funnel axis is not aligned with the orbital axis. In both cases, the orbital variations arise from the asymmetry of the funnel itself. The first model does not reproduce the strength of the signal in Stokes U because for a narrow funnel, most of the reflected photons that reach the observer are scattered at nearly the same angle, even for the additional part of funnel surface producing geometrical asymmetry. The second case is reminiscent to the rotating vector model, which has tight relation between the PD and PA variations. In order to reproduce the phase shift between the observed PD and PA variations, we find that the funnel should be inclined in the direction of movement in the orbit. On the contrary, the funnel moving through the stellar wind is expected to be tilted in the direction opposite to its velocity vector. Hence, we conclude that the variations in U are not caused by the asymmetric shape of the funnel itself.

Accretion geometry of Cyg X-3 and other high-mass X-ray binaries contains a common component, the bow shock produced by the movement of the compact object through the wind of the companion. The outflow from the compact object is expected to collide with the wind of the WR star, producing an enhanced density region. Presence of the bow shock in Cyg X-3 has been exploited to explain orbital changes of X-ray and IR fluxes [23]. We suggest that the high-amplitude orbital variability of PA seen both during the Main and ToO observations is produced thanks to the scattering of the scattered and reprocessed radiation of funnel walls from the inner surface of the
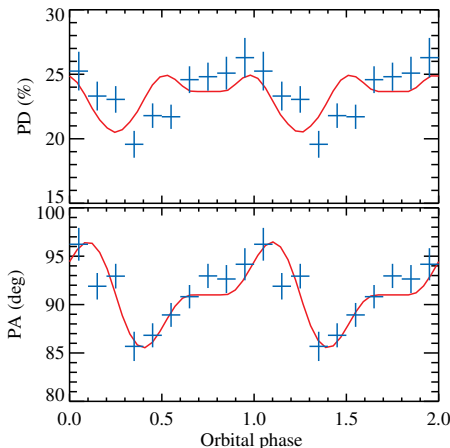
Fig. A12 Modelling orbital variations of the PD and PA. The blue crosses show the PD and PA for the Main observation in the 3.5–6 keV band and the red curve is the model of the reflection from a bow shock.

bow shock. In contrast to the beamed X-ray emission escaping along the funnel, the reflected and reprocessed light of the funnel walls is more isotropic. A fraction η_{bow} of the funnel radiation is scattered by the bow shock. We approximate its surface by a cylindrical sector parameterised by the angular extent ϕ_{cyl}, the azimuth of its centre at phase 0 (superior conjunction) relative to the line connecting the stars ϕ_{cen}, and by the height-to-radius ratio of the cylinder $H_{\mathrm{cyl}}/\rho_{\mathrm{cyl}}$. In this combined geometry with the funnel and the bow shock, the average polarization comes from the radiation reflected from the funnel (described by the parameters α and R) and the orbital variability arises from the scattering of mostly isotropic radiation off the inner surface of the bow shock (with parameters η_{bow}, ϕ_{cyl} and $H_{\mathrm{cyl}}/\rho_{\mathrm{cyl}}$). In Fig. A12 we show an example of description of orbital variations for parameters $\alpha = 10°$, $R = 50$, $H_{\mathrm{cyl}}/\rho_{\mathrm{cyl}} = 1$, $\phi_{\mathrm{cyl}} = 220°$, $\phi_{\mathrm{cen}} = 90°$ (at superior conjunction, the centre is located to the left of the line connecting the stars) and $\eta_{\mathrm{bow}} = 0.09$. We see, however, that the model does not reproduce the shape of PD exactly, and attribute this to the simplicity of the assumed bow shock geometry.

For our parameter $\phi_{\mathrm{cen}} = 90°$, the bow shock is located at maximal angular distances from the plane formed by the observer, the WR star and the compact object at conjunction phases. In other words, we expect the PA to be maximal/minimal at the conjunctions and cross its average value, $\sim 90°$, close to quadratures. From the fact that PA is maximal in the first orbital bin, we deduce that the Cyg X-3 system rotates in the counterclockwise direction.

A.3.2 Monte-Carlo modelling of the funnel

To consider the effects of finite optical depth and dependence of the resulting polarization on geometry, we ran Monte-Carlo (MC) simulations using the code STOKES version 2.07 [75, 76]. The code traces polarization of photons
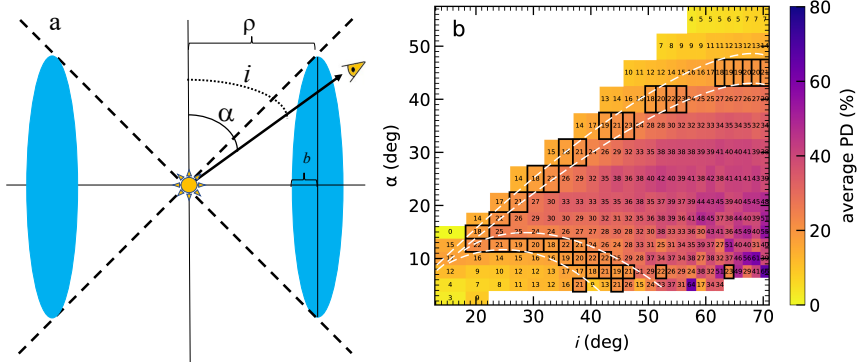
Fig. A13 Results of Monte-Carlo simulations. (a) The geometry of the reflector (elliptical torus in blue) and main parameters of the funnel explored by the Monte-Carlo modelling. **(b)** The simulated 2–8 keV PD versus observer's inclination and half-opening angle of the torus for $b = \rho/4$, $\tau_e = 7$ and $N_H = 10^{25}\,\mathrm{cm^{-2}}$ (the same display as in Fig. 3 for the analytical model). The black rectangles and white dashed lines mark the approximate estimate of the reprocessed funnel component from the data, i.e. PD = 21 ± 3 %.

propagating in media, taking into account the effects of photoelectric absorption and Compton down-scattering. Both continuum and line emission are considered. Our goal is to identify the parameter space for which the average observed polarization can be reproduced. The geometries reminiscent of the super-Eddington outflow that STOKES allows for are: (i) elliptical torus and (ii) wedge-shaped torus. We choose the first option of elliptical torus (see Fig. A13a for a geometry sketch), which should be more distinct from the cone-shaped outflow that we described in previous section. The profile of the torus is parameterised through the cylindrical distance ρ, the grazing angle α that corresponds the opening angle of the funnel in the cone geometry, and the minor axis b. Only the ratios of distances affect polarization properties. The point-like source located at the center of the coordinate system illuminates the axially symmetric scattering region.

The densities and atomic properties within the equatorial scattering region are homogeneous; column density along the scatterer is a function of observer inclination and is proportional to the length of the scattering region. We assume solar abundance from [77] with $A_{\mathrm{Fe}} = 1.0$. The main parameters of the medium that control polarization properties are the hydrogen number density, expressed through the column density N_H, and the number density of free electrons in the medium (related to ionization), defined through the electron-scattering Thomson optical depth τ_e. We show the results for the unpolarized primary radiation, but tested various cases of polarized primary emission. The same holds for the primary spectral distribution, which we fix as a power law with the photon index $\Gamma = 2$ for simplicity.

As an example, in Fig. A13b we show the 2–8 keV integrated PD as a function of the observer inclination i and the ellipse grazing angle α for the case $N_H = 10^{25}$ cm^{-2} and $\tau_e = 7$, corresponding to the partially ionized case

with nearly equal number densities of hydrogen and free electrons. The white dashed curves represent contours corresponding to the PD$\approx 21 \pm 3\%$ in the 2–8 keV range, where the lower and upper limits correspond to the character-istic uncertainties of the simulations. Cells with PD that falls in the correct range are also highlighted with black rectangles. We find that the contours form the same topology in the (i, α) space as for the analytical model and give similar, within uncertainties, allowed combinations of (i, α). We explored the parameter space with various aspect ratios, and compared the multiple-scattering to single-scattering cases. In all cases, we have been able to obtain a general pattern of two solutions, similar to the two branches in Fig. 3b. At 3.5–6 keV we obtained almost no difference between the single-scattering and multiple-scattering cases, as in these energies the single-scattering albedo is low.

A.4   Intrinsic and apparent luminosity estimates

Using analytical model described above, we can compute the luminosity escap-ing in the direction along the funnel axis L_{ULX} from the observed flux. We assume that the primary X-ray source within the funnel is isotropic and pro-duces luminosity L_{X}. In this case, the luminosity escaping in a given solid angle is proportional to this solid angle, $L_{\Omega} \propto \Omega$. Three distinct sites of contribute to total X-ray luminosity: the funnel opening, where the fraction proportional to the solid angle of the funnel escapes, the reprocessing cite seen to the observer (region between point L and upper boundary of the funnel in Fig. A11) and the lower layers of the funnel (between point L and the disc plane). The con-tribution of the latter luminosity may come in the form of a soft reprocessed X-ray radiation and is not well visible in our data. The contribution of the former two can be related to the intrinsic X-ray luminosity:

$$L_{\text{ULX}} = \frac{2\pi}{\Omega_{\text{ULX}}} L_{\text{X}}, \tag{A3}$$

where $\Omega_{\text{ULX}} = 2\pi(1 - \cos\alpha)$ is the solid angle of the funnel opening as seen from the primary X-ray source. The observer receives the flux F_{obs}, which is emitted by (reflected from) the visible part of the inner surface of the funnel (geometry in Fig. A11). The luminosity intercepted by this part can be expressed through the luminosity of the primary X-ray source as

$$L_{\text{refl}} = \frac{\Omega_{\text{refl}}}{\Omega_{\text{ULX}}} a L_{\text{X}}, \tag{A4}$$

where a is the scattering albedo and Ω_{refl} is the characteristic solid angle of the reflecting surface (that is the observer is able to see), as viewed from the primary X-ray source. The reflected luminosity produces the observed flux we detect, hence $F_{\text{obs}} = L_{\text{refl}}/(4\pi D^2)$. Combining the terms, we can get the

expression for the luminosity escaping along the funnel:

$$L_{\mathrm{ULX}} = \frac{2\pi}{\Omega_{\mathrm{refl}}} \frac{4\pi D^2 F_{\mathrm{obs}}}{a}. \tag{A5}$$

The solid angle of the reflecting surface can be expressed as

$$\frac{\Omega_{\mathrm{refl}}}{2\pi} = \cos\alpha - \cos\alpha^*, \tag{A6}$$

where α^* corresponds to the angle at which the lowest interior part of the funnel is seen to an observer (Fig. A11). This angle is related to the funnel opening angle ζ as

$$\tan\alpha^* = \frac{\tan\zeta}{1 - 1/\rho_{\mathrm{L}}}, \tag{A7}$$

$\rho_{\min}$ is the radius of the funnel at point L, in units of inner radii of the outflow. It can be expressed through the model parameter α, the cylindrical radius of the funnel outer boundary $\rho = R\sin\alpha$ and the observer inclination i as

$$\frac{1}{\rho_{\mathrm{L}}} = \frac{1}{\rho} \frac{\tan i + \tan\zeta}{\tan i - \tan\zeta}. \tag{A8}$$

The opening angle is in turn related to the model parameter α as

$$\tan\zeta = (1 - 1/\rho)\tan\alpha. \tag{A9}$$

Substituting Eq. (A8) and (A9) into Eq. (A7) and expressing $\cos\alpha^*$, we can find $\Omega_{\mathrm{refl}}/2\pi$ as a function of parameters ρ, α and i. Further, for the given observed polarization we can relate α and R (see red contour in Fig. A11), which makes $\Omega_{\mathrm{refl}}/2\pi$ only a function of α. In Fig. A14 (solid red line) we show that, for all combinations (α, R) which give the observed polarization, we find $\Omega_{\mathrm{refl}}/2\pi \lesssim 2\times 10^{-2}$.

We take the observed flux before accounting for the absorption in the WR wind and along the line of sight in the Galaxy as a lower limit on $F_{\mathrm{obs}} = 1.53\times10^{-9}$ erg cm^{-2} s^{-1}. Albedo is a function of energy, abundance and viewing angle [78]. Motivated by our spectral fitting (Fig. A7) we take the value $a \sim 0.1$ as a conservative approximation. Inserting the numbers into Eq. (A5), we get a lower limit on the luminosity seen along the funnel in the 2–8 keV range, $L_{\mathrm{ULX}} \approx 5\times 10^{39}$ erg s^{-1}.

To estimate the intrinsic X-ray luminosity, we need to take into account several additional factors. First, the observed fluxes have to be corrected for absorption. For our spectropolarimetric modelling, the unabsorbed flux in IXPE band is $F_{\mathrm{unabs}} = 2.6\times 10^{-9}$ erg cm^{-2} s^{-1}. Further, we need to take into account the bolometric luminosity correction, f_{bol}. For the soft intrinsic X-ray spectra we obtain in our spectral fitting (Fig. A7), we estimate this factor $f_{\mathrm{bol}} \sim 2 - 3$. Finally, we can slightly relax the assumption of the minimal R
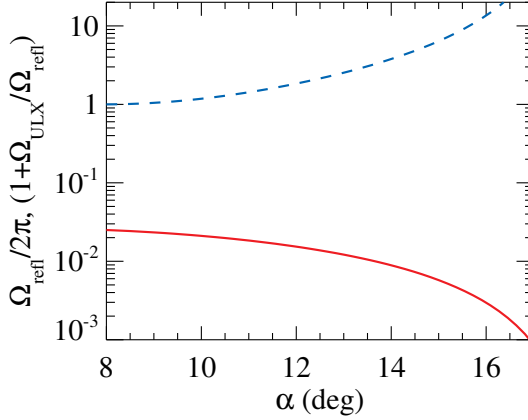
Fig. A14 Reflection and amplification factors. Dependence of the solid angle of the reflecting surface (red solid curve) and the factor determining the intrinsic luminosity (blue dashed curve) on angle α.

and consider the range of luminosities for different α. The intrinsic bolometric X-ray luminosity can be expressed through the unabsorbed X-ray flux as

$$L_{\rm X,bol} = \frac{4\pi D^2 f_{\rm bol} F_{\rm unabs}}{a} \left(1 + \frac{\Omega_{\rm ULX}}{\Omega_{\rm refl}}\right) \approx 5\times10^{38} \left(1 + \frac{1 - \cos\zeta}{\Omega_{\rm refl}/2\pi}\right) {\rm erg\ s^{-1}}. \quad \text{(A10)}$$

In Fig. A14 (blue dashed line) we show the dependence of the amplification factor $(1 + \Omega_{\rm ULX}/\Omega_{\rm refl})$ on the angle α. The obtained luminosity can be compared to the Eddington accretion rate for He (given that the source shows hydrogen-poor properties [17]) $L_{\rm Edd,He} = 2.6 \times 10^{38}(M_{\rm X}/M_\odot)$ erg s^{-1} (where $M_{\rm X}$ is the mass of the compact object and $M_\odot$ is the solar mass). We obtain that for small funnel angles, $\alpha \approx 8°$, the intrinsic bolometric X-ray luminosity exceeds the Eddington limit only for a compact object with low mass, $M_{\rm X}/M_\odot \lesssim 2$, suggesting its neutron star origin. For a slightly higher $\alpha \approx 16°$, the observed limit exceed the Eddington limit even for $M_{\rm X}/M_\odot \approx 20$, which corresponds to the heaviest Galactic black hole mass measured today [79]. Interestingly, for the case when scattering proceeds in the optically thin wind above the funnel, but the factor in brackets should be replaced with $1/\tau_{\rm T,WR} \approx 2 - 10$, which does not affect the final estimate of intrinsic luminosity.

If the source is surrounded by the envelope with narrow funnel, the primary luminosity will be beamed in the direction along its axis. From the obtained geometry, we can directly get the geometrical amplification (beaming) factor,

$$b = \frac{1}{1 - \cos\zeta} \gtrsim 65. \quad \text{(A11)}$$

The beaming is expected to vary with the opening angle and can ultimately depend on the mass accretion rate [80]. More precise estimates of the beaming factor can be obtained using proper calculations of the photons interactions
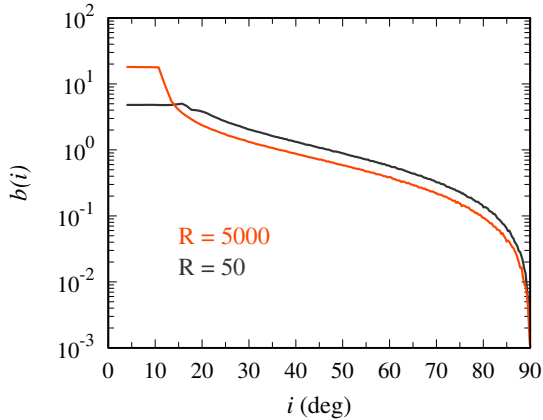
Fig. A15 Beaming factor dependence on inclination. The dependence of the beaming factor b on the inclination angle i for the case of the funnel of opening angle $\zeta = 10°$. The black and red curves correspond to the different heights of the funnel $R = 50$ and 5000, respectively. In both cases, the strongest beaming is expected within the opening angle on the funnel, and the beaming factor drops down to zero at $i = 90°$.

with the funnel walls [81]. We performed Monte-Carlo simulations of multiple reflection and reprocessing events within the funnel and find (see Fig. A15) that a substantial fraction of photons leave the system outside of the solid angle Ω_{ULX}, i.e. that the beaming factor is reduced, as compared to the simple geometrical estimate in Eq. (A11). The magnitude of reduction, in turn, depends on the height of the funnel: larger number of photons leave the system outside of Ω_{ULX} for larger R. The estimate in Eq. (A11) corresponds to the limiting case of infinitely large R (even $b \approx 20$ requires $R \approx 90$ for $\zeta = 10°$). We can now estimate the effective temperature of radiation reprocessed by the walls and detectable by a distant observer. The local effective temperature of the funnel wall is determined by the total absorbed X-ray energy flux. The apparent luminosity in a given direction $b(i)L_{\mathrm{X}}$ is emitted by the part of the funnel of the projected area $\pi\rho^2 \cos i$ that is visible to a distant observer. Thus we can estimate the surface effective temperature as:

$$T_{\mathrm{funnel}} \simeq \left[\frac{(1-a)b(i)L_{\mathrm{X}}}{4\pi\sigma_{\mathrm{SB}}\cos i} \frac{1}{R^2 \sin^2\alpha} \right]^{1/4} \tag{A12}$$

$$\approx 0.3 \left(\frac{b(i)L_{\mathrm{X}}}{10^{39}\,\mathrm{erg\,s^{-1}}} \right)^{1/4} \left(\frac{R}{10^8\,\mathrm{cm}} \right)^{-1/2} \left(\frac{1}{\cos i \sin^2\alpha} \right)^{1/4} \mathrm{keV}.$$

Interestingly, the obtained radiation-supported funnel temperature structure has the same radial scaling relation as expected in ULXs [30], and the characteristic values are in line with the temperatures of the thermal components observed in ULX sources [1]. This indicates that the soft thermal component we see in the IXPE data agrees with the radiation of the funnel walls.

References

[1] Kaaret, P., Feng, H., Roberts, T.P.: Ultraluminous X-Ray Sources. ARA&A **55**(1), 303–341 (2017) arXiv:1703.10728 [astro-ph.HE]. https://doi.org/10.1146/annurev-astro-091916-055259

[2] Weisskopf, M.C., Soffitta, P., Baldini, L., Ramsey, B.D., O'Dell, S.L., Romani, R.W., Matt, G., Deininger, W.D., Baumgartner, W.H., Bellazzini, R., Costa, E., Kolodziejczak, J.J., Latronico, L., Marshall, H.L., Muleri, F., Bongiorno, S.D., Tennant, A., Bucciantini, N., Dovciak, M., Marin, F., Marscher, A., Poutanen, J., Slane, P., Turolla, R., Kalinowski, W., Di Marco, A., Fabiani, S., Minuti, M., La Monaca, F., Pinchera, M., Rankin, J., Sgro', C., Trois, A., Xie, F., Alexander, C., Allen, D.Z., Amici, F., Andersen, J., Antonelli, A., Antoniak, S., Attinà, P., Barbanera, M., Bachetti, M., Baggett, R.M., Bladt, J., Brez, A., Bonino, R., Boree, C., Borotto, F., Breeding, S., Brienza, D., Bygott, H.K., Caporale, C., Cardelli, C., Carpentiero, R., Castellano, S., Castronuovo, M., Cavalli, L., Cavazzuti, E., Ceccanti, M., Centrone, M., Citraro, S., D'Amico, F., D'Alba, E., Di Gesu, L., Del Monte, E., Dietz, K.L., Di Lalla, N., Persio, G.D., Dolan, D., Donnarumma, I., Evangelista, Y., Ferrant, K., Ferrazzoli, R., Ferrie, M., Footdale, J., Forsyth, B., Foster, M., Garelick, B., Gunji, S., Gurnee, E., Head, M., Hibbard, G., Johnson, S., Kelly, E., Kilaru, K., Lefevre, C., Roy, S.L., Loffredo, P., Lorenzi, P., Lucchesi, L., Maddox, T., Magazzu, G., Maldera, S., Manfreda, A., Mangraviti, E., Marengo, M., Marrocchesi, A., Massaro, F., Mauger, D., McCracken, J., McEachen, M., Mize, R., Mereu, P., Mitchell, S., Mitsuishi, I., Morbidini, A., Mosti, F., Nasimi, H., Negri, B., Negro, M., Nguyen, T., Nitschke, I., Nuti, A., Onizuka, M., Oppedisano, C., Orsini, L., Osborne, D., Pacheco, R., Paggi, A., Painter, W., Pavelitz, S.D., Pentz, C., Piazzolla, R., Perri, M., Pesce-Rollins, M., Peterson, C., Pilia, M., Profeti, A., Puccetti, S., Ranganathan, J., Ratheesh, A., Reedy, L., Root, N., Rubini, A., Ruswick, S., Sanchez, J., Sarra, P., Santoli, F., Scalise, E., Sciortino, A., Schroeder, C., Seek, T., Sosdian, K., Spandre, G., Speegle, C.O., Tamagawa, T., Tardiola, M., Tobia, A., Thomas, N.E., Valerie, R., Vimercati, M., Walden, A.L., Weddendorf, B., Wedmore, J., Welch, D., Zanetti, D., Zanetti, F.: The Imaging X-Ray Polarimetry Explorer (IXPE): Pre-Launch. Journal of Astronomical Telescopes, Instruments, and Systems **8**(2), 026002 (2022) arXiv:2112.01269 [astro-ph.IM]. https://doi.org/10.1117/1.JATIS.8.2.026002

[3] Giacconi, R., Gorenstein, P., Gursky, H., Waters, J.R.: An X-Ray Survey of the Cygnus Region. ApJ **148**, 119 (1967). https://doi.org/10.1086/180028

[4] Gregory, P.C., Kronberg, P.P.: Discovery of Giant Radio Outburst from Cygnus X-3. Nature **239**(5373), 440–443 (1972). https://doi.org/10.1038/

239440a0

[5] McCollough, M.L., Robinson, C.R., Zhang, S.N., Harmon, B.A., Hjellming, R.M., Waltman, E.B., Foster, R.S., Ghigo, F.D., Briggs, M.S., Pendleton, G.N., Johnston, K.J.: Discovery of Correlated Behavior between the Hard X-Ray and the Radio Bands in Cygnus X-3. ApJ **517**(2), 951–955 (1999) arXiv:astro-ph/9810212 [astro-ph]. https://doi.org/10.1086/307241

[6] Atwood, W.B., Abdo, A.A., Ackermann, M., Althouse, W., Anderson, B., Axelsson, M., Baldini, L., Ballet, J., Band, D.L., Barbiellini, G., Bartelt, J., Bastieri, D., Baughman, B.M., Bechtol, K., Bédérède, D., Bellardi, F., Bellazzini, R., Berenji, B., Bignami, G.F., Bisello, D., Bissaldi, E., Blandford, R.D., Bloom, E.D., Bogart, J.R., Bonamente, E., Bonnell, J., Borgland, A.W., Bouvier, A., Bregeon, J., Brez, A., Brigida, M., Bruel, P., Burnett, T.H., Busetto, G., Caliandro, G.A., Cameron, R.A., Caraveo, P.A., Carius, S., Carlson, P., Casandjian, J.M., Cavazzuti, E., Ceccanti, M., Cecchi, C., Charles, E., Chekhtman, A., Cheung, C.C., Chiang, J., Chipaux, R., Cillis, A.N., Ciprini, S., Claus, R., Cohen-Tanugi, J., Condamoor, S., Conrad, J., Corbet, R., Corucci, L., Costamante, L., Cutini, S., Davis, D.S., Decotigny, D., DeKlotz, M., Dermer, C.D., de Angelis, A., Digel, S.W., do Couto e Silva, E., Drell, P.S., Dubois, R., Dumora, D., Edmonds, Y., Fabiani, D., Farnier, C., Favuzzi, C., Flath, D.L., Fleury, P., Focke, W.B., Funk, S., Fusco, P., Gargano, F., Gasparrini, D., Gehrels, N., Gentit, F.-X., Germani, S., Giebels, B., Giglietto, N., Giommi, P., Giordano, F., Glanzman, T., Godfrey, G., Grenier, I.A., Grondin, M.-H., Grove, J.E., Guillemot, L., Guiriec, S., Haller, G., Harding, A.K., Hart, P.A., Hays, E., Healey, S.E., Hirayama, M., Hjalmarsdotter, L., Horn, R., Hughes, R.E., Jóhannesson, G., Johansson, G., Johnson, A.S., Johnson, R.P., Johnson, T.J., Johnson, W.N., Kamae, T., Katagiri, H., Kataoka, J., Kavelaars, A., Kawai, N., Kelly, H., Kerr, M., Klamra, W., Knödlseder, J., Kocian, M.L., Komin, N., Kuehn, F., Kuss, M., Landriu, D., Latronico, L., Lee, B., Lee, S.-H., Lemoine-Goumard, M., Lionetto, A.M., Longo, F., Loparco, F., Lott, B., Lovellette, M.N., Lubrano, P., Madejski, G.M., Makeev, A., Marangelli, B., Massai, M.M., Mazziotta, M.N., McEnery, J.E., Menon, N., Meurer, C., Michelson, P.F., Minuti, M., Mirizzi, N., Mitthumsiri, W., Mizuno, T., Moiseev, A.A., Monte, C., Monzani, M.E., Moretti, E., Morselli, A., Moskalenko, I.V., Murgia, S., Nakamori, T., Nishino, S., Nolan, P.L., Norris, J.P., Nuss, E., Ohno, M., Ohsugi, T., Omodei, N., Orlando, E., Ormes, J.F., Paccagnella, A., Paneque, D., Panetta, J.H., Parent, D., Pearce, M., Pepe, M., Perazzo, A., Pesce-Rollins, M., Picozza, P., Pieri, L., Pinchera, M., Piron, F., Porter, T.A., Poupard, L., Rainò, S., Rando, R., Rapposelli, E., Razzano, M., Reimer, A., Reimer, O., Reposeur, T., Reyes, L.C., Ritz, S., Rochester, L.S., Rodriguez, A.Y., Romani, R.W., Roth, M., Russell, J.J., Ryde, F., Sabatini, S., Sadrozinski, H.F.-W., Sanchez, D., Sander, A.,

Sapozhnikov, L., Parkinson, P.M.S., Scargle, J.D., Schalk, T.L., Scolieri, G., Sgrò, C., Share, G.H., Shaw, M., Shimokawabe, T., Shrader, C., Sierpowska-Bartosik, A., Siskind, E.J., Smith, D.A., Smith, P.D., Spandre, G., Spinelli, P., Starck, J.-L., Stephens, T.E., Strickman, M.S., Strong, A.W., Suson, D.J., Tajima, H., Takahashi, H., Takahashi, T., Tanaka, T., Tenze, A., Tether, S., Thayer, J.B., Thayer, J.G., Thompson, D.J., Tibaldo, L., Tibolla, O., Torres, D.F., Tosti, G., Tramacere, A., Turri, M., Usher, T.L., Vilchez, N., Vitale, V., Wang, P., Watters, K., Winer, B.L., Wood, K.S., Ylinen, T., Ziegler, M.: The Large Area Telescope on the Fermi Gamma-Ray Space Telescope Mission. ApJ **697**(2), 1071–1102 (2009) arXiv:0902.1089 [astro-ph.IM]. https://doi.org/10.1088/0004-637X/697/2/1071

[7] Tavani, M., Bulgarelli, A., Piano, G., Sabatini, S., Striani, E., Evangelista, Y., Trois, A., Pooley, G., Trushkin, S., Nizhelskij, N.A., McCollough, M., Koljonen, K.I.I., Pucella, G., Giuliani, A., Chen, A.W., Costa, E., Vittorini, V., Trifoglio, M., Gianotti, F., Argan, A., Barbiellini, G., Caraveo, P., Cattaneo, P.W., Cocco, V., Contessi, T., D'Ammando, F., Del Monte, E., de Paris, G., Di Cocco, G., di Persio, G., Donnarumma, I., Feroci, M., Ferrari, A., Fuschino, F., Galli, M., Labanti, C., Lapshov, I., Lazzarotto, F., Lipari, P., Longo, F., Mattaini, E., Marisaldi, M., Mastropietro, M., Mauri, A., Mereghetti, S., Morelli, E., Morselli, A., Pacciani, L., Pellizzoni, A., Perotti, F., Picozza, P., Pilia, M., Prest, M., Rapisarda, M., Rappoldi, A., Rossi, E., Rubini, A., Scalise, E., Soffitta, P., Vallazza, E., Vercellone, S., Zambra, A., Zanello, D., Pittori, C., Verrecchia, F., Giommi, P., Colafrancesco, S., Santolamazza, P., Antonelli, A., Salotti, L.: Extreme particle acceleration in the microquasar CygnusX-3. Nature **462**(7273), 620–623 (2009) arXiv:0910.5344 [astro-ph.HE]. https://doi.org/10.1038/nature08578

[8] Lommen, D., Yungelson, L., van den Heuvel, E., Nelemans, G., Portegies Zwart, S.: Cygnus X-3 and the problem of the missing Wolf-Rayet X-ray binaries. A&A **443**(1), 231–241 (2005) arXiv:astro-ph/0507304 [astro-ph]. https://doi.org/10.1051/0004-6361:20052824

[9] Belczynski, K., Bulik, T., Mandel, I., Sathyaprakash, B.S., Zdziarski, A.A., Mikołajewska, J.: Cyg X-3: A Galactic Double Black Hole or Black-hole-Neutron-star Progenitor. ApJ **764**(1), 96 (2013) arXiv:1209.2658 [astro-ph.HE]. https://doi.org/10.1088/0004-637X/764/1/96

[10] van Kerkwijk, M.H., Charles, P.A., Geballe, T.R., King, D.L., Miley, G.K., Molnar, L.A., van den Heuvel, E.P.J., van der Klis, M., van Paradijs, J.: Infrared helium emission lines from Cygnus X-3 suggesting a Wolf-Rayet star companion. Nature **355**(6362), 703–705 (1992). https://doi.org/10.1038/355703a0

[11] van Kerkwijk, M.H., Geballe, T.R., King, D.L., van der Klis, M., van Paradijs, J.: The Wolf-Rayet counterpart of Cygnus X-3. A&A **314**, 521–540 (1996) arXiv:astro-ph/9604100 [astro-ph]

[12] McCollough, M.L., Corrales, L., Dunham, M.M.: Cygnus X-3: Its Little Friend's Counterpart, the Distance to Cygnus X-3, and Outflows/Jets. ApJ **830**(2), 36 (2016) arXiv:1610.01923 [astro-ph.HE]. https://doi.org/10.3847/2041-8205/830/2/L36

[13] Martí, J., Paredes, J.M., Peracaula, M.: The Cygnus X-3 Radio Jets at Arcsecond Scales. ApJ **545**(2), 939–944 (2000). https://doi.org/10.1086/317858

[14] Miller-Jones, J.C.A., Blundell, K.M., Rupen, M.P., Mioduszewski, A.J., Duffy, P., Beasley, A.J.: Time-sequenced Multi-Radio Frequency Observations of Cygnus X-3 in Flare. ApJ **600**(1), 368–389 (2004) arXiv:astro-ph/0311277 [astro-ph]. https://doi.org/10.1086/379706

[15] Jones, T.J., Gehrz, R.D., Kobulnicky, H.A., Molnar, L.A., Howard, E.M.: Infrared Photometry and Polarimetry of Cygnus X-3. AJ **108**, 605 (1994). https://doi.org/10.1086/117094

[16] Hjellming, R.M.: An Astronomical Puzzle Called Cygnus X-3. Science **182**(4117), 1089–1095 (1973). https://doi.org/10.1126/science.182.4117.1089

[17] Fender, R.P., Hanson, M.M., Pooley, G.G.: Infrared spectroscopic variability of Cygnus X-3 in outburst and quiescence. MNRAS **308**(2), 473–484 (1999) arXiv:astro-ph/9903435 [astro-ph]. https://doi.org/10.1046/j.1365-8711.1999.02726.x

[18] Vilhu, O., Hakala, P., Hannikainen, D.C., McCollough, M., Koljonen, K.: Orbital modulation of X-ray emission lines in Cygnus X-3. A&A **501**(2), 679–686 (2009) arXiv:0904.3967 [astro-ph.HE]. https://doi.org/10.1051/0004-6361/200811293

[19] Kallman, T., McCollough, M., Koljonen, K., Liedahl, D., Miller, J., Paerels, F., Pooley, G., Sako, M., Schulz, N., Trushkin, S., Corrales, L.: Photoionization Emission Models for the Cyg X-3 X-Ray Spectrum. ApJ **874**(1), 51 (2019) arXiv:1902.05589 [astro-ph.HE]. https://doi.org/10.3847/1538-4357/ab09f8

[20] van der Klis, M., Bonnet-Bidaud, J.M.: A change in light curve asymmetry and the ephemeris of CYG X-3. A&A **95**, 5–7 (1981)

[21] Antokhin, I.I., Cherepashchuk, A.M.: The Period Change of Cyg X-3. ApJ **871**(2), 244 (2019) arXiv:1807.00817 [astro-ph.HE]. https://doi.org/

10.3847/1538-4357/aafb38

[22] Mioduszewski, A.J., Rupen, M.P., Hjellming, R.M., Pooley, G.G., Walt-man, E.B.: A One-sided Highly Relativistic Jet from Cygnus X-3. ApJ **553**(2), 766–775 (2001) arXiv:astro-ph/0102018 [astro-ph]. https://doi.org/10.1086/320965

[23] Antokhin, I.I., Cherepashchuk, A.M., Antokhina, E.A., Tatarnikov, A.M.: Near-IR and X-Ray Variability of Cyg X-3: Evidence for a Compact IR Source and Complex Wind Structures. ApJ **926**(2), 123 (2022) arXiv:2112.04805 [astro-ph.HE]. https://doi.org/10.3847/1538-4357/ac4047

[24] Szostek, A., Zdziarski, A.A., McCollough, M.L.: A classification of the X-ray and radio states of Cyg X-3 and their long-term correlations. MNRAS **388**(3), 1001–1010 (2008) arXiv:0803.2217 [astro-ph]. https://doi.org/10.1111/j.1365-2966.2008.13479.x

[25] Zdziarski, A.A., Misra, R., Gierliński, M.: Compton scattering as the explanation of the peculiar X-ray properties of Cyg X-3. MNRAS **402**(2), 767–775 (2010) arXiv:0905.1086 [astro-ph.HE]. https://doi.org/10.1111/j.1365-2966.2009.15942.x

[26] Hjalmarsdotter, L., Zdziarski, A.A., Larsson, S., Beckmann, V., McCol-lough, M., Hannikainen, D.C., Vilhu, O.: The nature of the hard state of Cygnus X-3. MNRAS **384**(1), 278–290 (2008) arXiv:0707.2032 [astro-ph]. https://doi.org/10.1111/j.1365-2966.2007.12688.x

[27] Brown, J.C., McLean, I.S., Emslie, A.G.: Polarisation by Thomson scat-tering in optically thin stellar envelopes. II. Binary and multiple star envelopes and the determination of binary inclinations. A&A **68**, 415–427 (1978)

[28] Ursini, F., Marinucci, A., Matt, G., Bianchi, S., Marin, F., Marshall, H.L., Middei, R., Poutanen, J., Rogantini, D., De Rosa, A., Di Gesu, L., García, J.A., Ingram, A., Kim, D.E., Krawczynski, H., Puccetti, S., Soffitta, P., Svoboda, J., Tombesi, F., Weisskopf, M.C., Barnouin, T., Perri, M., Pod-gorny, J., Ratheesh, A., Zaino, A., Agudo, I., Antonelli, L.A., Bachetti, M., Baldini, L., Baumgartner, W.H., Bellazzini, R., Bongiorno, S.D., Bonino, R., Brez, A., Bucciantini, N., Capitanio, F., Castellano, S., Cavazzuti, E., Ciprini, S., Costa, E., Del Monte, E., Di Lalla, N., Di Marco, A., Donnarumma, I., Doroshenko, V., Dovciak, M., Ehlert, S.R., Enoto, T., Evangelista, Y., Fabiani, S., Ferrazzoli, R., Gunji, S., Heyl, J., Iwakiri, W., Jorstad, S.G., Karas, V., Kitaguchi, T., Kolodziejczak, J.J., La Monaca, F., Latronico, L., Liodakis, I., Maldera, S., Manfreda, A., Marscher, A.P., Mitsuishi, I., Mizuno, T., Muleri, F., Ng, C.Y., O'Dell, S.L., Omodei, N., Oppedisano, C., Papitto, A., Pavlov, G.G., Peirson, A.L., Pesce-Rollins,

M., Petrucci, P.-O., Pilia, M., Possenti, A., Ramsey, B.D., Rankin, J., Romani, R.W., Sgrò, C., Slane, P., Spandre, G., Tamagawa, T., Tavecchio, F., Taverna, R., Tawara, Y., Tennant, A.F., Thomas, N.E., Trois, A., Tsygankov, S.S., Turolla, R., Vink, J., Wu, K., Xie, F., Zane, S.: Mapping the circumnuclear regions of the Circinus galaxy with the Imaging X-ray Polarimetry Explorer. MNRAS **519**(1), 50–58 (2023) arXiv:2211.01697 [astro-ph.HE]. https://doi.org/10.1093/mnras/stac3189

[29] Shakura, N.I., Sunyaev, R.A.: Black holes in binary systems. Observational appearance. A&A **24**, 337–355 (1973)

[30] Poutanen, J., Lipunova, G., Fabrika, S., Butkevich, A.G., Abolmasov, P.: Supercritically accreting stellar mass black holes as ultraluminous X-ray sources. MNRAS **377**(3), 1187–1194 (2007) arXiv:astro-ph/0609274 [astro-ph]. https://doi.org/10.1111/j.1365-2966.2007.11668.x

[31] Long, K.S., Chanan, G.A., Novick, R.: The X-ray polarization of the CYG sources. ApJ **238**, 710–716 (1980). https://doi.org/10.1086/158027

[32] Krawczynski, H., Muleri, F., Dovčiak, M., Veledina, A., Rodriguez Cavero, N., Svoboda, J., Ingram, A., Matt, G., Garcia, J.A., Loktev, V., Negro, M., Poutanen, J., Kitaguchi, T., Podgorný, J., Rankin, J., Zhang, W., Berdyugin, A., Berdyugina, S.V., Bianchi, S., Blinov, D., Capitanio, F., Di Lalla, N., Draghis, P., Fabiani, S., Kagitani, M., Kravtsov, V., Kiehlmann, S., Latronico, L., Lutovinov, A.A., Mandarakas, N., Marin, F., Marinucci, A., Miller, J.M., Mizuno, T., Molkov, S.V., Omodei, N., Petrucci, P.-O., Ratheesh, A., Sakanoi, T., Semena, A.N., Skalidis, R., Soffitta, P., Tennant, A.F., Thalhammer, P., Tombesi, F., Weisskopf, M.C., Wilms, J., Zhang, S., Agudo, I., Antonelli, L.A., Bachetti, M., Baldini, L., Baumgartner, W.H., Bellazzini, R., Bongiorno, S.D., Bonino, R., Brez, A., Bucciantini, N., Castellano, S., Cavazzuti, E., Ciprini, S., Costa, E., De Rosa, A., Del Monte, E., Di Gesu, L., Di Marco, A., Donnarumma, I., Doroshenko, V., Ehlert, S.R., Enoto, T., Evangelista, Y., Ferrazzoli, R., Gunji, S., Hayashida, K., Heyl, J., Iwakiri, W., Jorstad, S.G., Karas, V., Kolodziejczak, J.J., La Monaca, F., Liodakis, I., Maldera, S., Manfreda, A., Marscher, A.P., Marshall, H.L., Mitsuishi, I., Ng, C.-Y., O'Dell, S.L., Oppedisano, C., Papitto, A., Pavlov, G.G., Peirson, A.L., Perri, M., Pesce-Rollins, M., Pilia, M., Possenti, A., Puccetti, S., Ramsey, B.D., Romani, R.W., Sgrò, C., Slane, P., Spandre, G., Tamagawa, T., Tavecchio, F., Taverna, R., Tawara, Y., Thomas, N.E., Trois, A., Tsygankov, S., Turolla, R., Vink, J., Wu, K., Xie, F., Zane, S.: Polarized x-rays constrain the disk-jet geometry in the black hole x-ray binary Cygnus X-1. Science **378**(6620), 650–654 (2022) arXiv:2206.09972 [astro-ph.HE]. https://doi.org/10.1126/science.add5399

[33] Di Marco, A., Soffitta, P., Costa, E., Ferrazzoli, R., La Monaca, F.,

Rankin, J., Ratheesh, A., Xie, F., Baldini, L., Del Monte, E., Ehlert, S.R., Fabiani, S., Kim, D.E., Muleri, F., O'Dell, S.L., Ramsey, B.D., Rubini, A., Sgrò, C., Silvestri, S., Tennant, A.F., Weisskopf, M.C.: Handling Background in IXPE polarimetric data. AJ, in press (2023) arXiv:2302.02927 [astro-ph.IM]. https://doi.org/10.48550/arXiv.2302.02927

[34] Strohmayer, T.E.: X-Ray Spectro-polarimetry with Photoelectric Polarimeters. ApJ **838**(1), 72 (2017) arXiv:1703.00949 [astro-ph.IM]. https://doi.org/10.3847/1538-4357/aa643d

[35] Arnaud, K.A.: XSPEC: The First Ten Years. In: Jacoby, G.H., Barnes, J. (eds.) Astronomical Data Analysis Software and Systems V. Astronomical Society of the Pacific Conference Series, vol. 101, p. 17 (1996)

[36] Baldini, L., Bucciantini, N., Di Lalla, N., Ehlert, S.R., Manfreda, A., Omodei, N., Pesce-Rollins, M., Sgrò, C.: ixpeobssim: a Simulation and Analysis Framework for the Imaging X-ray Polarimetry Explorer. SoftwareX **19**, 101194 (2022) arXiv:2203.06384 [astro-ph.IM]. https://doi.org/10.1016/j.softx.2022.101194

[37] Kislat, F., Clark, B., Beilicke, M., Krawczynski, H.: Analyzing the data from X-ray polarimeters with Stokes parameters. Astroparticle Physics **68**, 45–51 (2015) arXiv:1409.6214 [astro-ph.IM]. https://doi.org/10.1016/j.astropartphys.2015.02.007

[38] Wilms, J., Allen, A., McCray, R.: On the Absorption of X-Rays in the Interstellar Medium. ApJ **542**(2), 914–924 (2000) arXiv:astro-ph/0008425 [astro-ph]. https://doi.org/10.1086/317016

[39] Koljonen, K.I.I., Hannikainen, D.C., McCollough, M.L., Pooley, G.G., Trushkin, S.A.: The hardness-intensity diagram of Cygnus X-3: revisiting the radio/X-ray states. MNRAS **406**(1), 307–319 (2010) arXiv:1003.4351 [astro-ph.HE]. https://doi.org/10.1111/j.1365-2966.2010.16722.x

[40] Zdziarski, A.A., Mikolajewska, J., Belczynski, K.: Cyg X-3: a low-mass black hole or a neutron star. MNRAS **429**, 104–108 (2013) arXiv:1208.5455 [astro-ph.HE]. https://doi.org/10.1093/mnrasl/sls035

[41] Koljonen, K.I.I., Maccarone, T.J.: Gemini/GNIRS infrared spectroscopy of the Wolf-Rayet stellar wind in Cygnus X-3. MNRAS **472**(2), 2181–2195 (2017) arXiv:1708.04050 [astro-ph.HE]. https://doi.org/10.1093/mnras/stx2106

[42] Suryanarayanan, A., Paerels, F., Leutenegger, M.: The High resolution Fe K Spectrum of Cygnus X-3. arXiv e-prints, 2212–04165 (2022) arXiv:2212.04165 [astro-ph.HE]

[43] Corbel, S., Dubus, G., Tomsick, J.A., Szostek, A., Corbet, R.H.D., Miller-Jones, J.C.A., Richards, J.L., Pooley, G., Trushkin, S., Dubois, R., Hill, A.B., Kerr, M., Max-Moerbeck, W., Readhead, A.C.S., Bodaghee, A., Tudose, V., Parent, D., Wilms, J., Pottschmidt, K.: A giant radio flare from Cygnus X-3 with associated γ-ray emission. MNRAS **421**(4), 2947–2955 (2012) arXiv:1201.3356 [astro-ph.HE]. https://doi.org/10.1111/j.1365-2966.2012.20517.x

[44] Egron, E., Pellizzoni, A., Righini, S., Giroletti, M., Koljonen, K., Pottschmidt, K., Trushkin, S., Lobina, J., Pilia, M., Wilms, J., Corbel, S., Grinberg, V., Loru, S., Trois, A., Rodriguez, J., Lähteenmäki, A., Tornikoski, M., Enestam, S., Järvelä, E.: Investigating the Mini and Giant Radio Flare Episodes of Cygnus X-3. ApJ **906**(1), 10 (2021) arXiv:2010.15002 [astro-ph.HE]. https://doi.org/10.3847/1538-4357/abc5b1

[45] Parsignault, D.R., Gursky, H., Kellogg, E.M., Matilsky, T., Murray, S., Schreier, E., Tananbaum, H., Giacconi, R., Brinkman, A.C.: Observations of Cygnus X-3 by Uhuru. Nature Physical Science **239**(95), 123–125 (1972). https://doi.org/10.1038/physci239123a0

[46] Bonnet-Bidaud, J.M., van der Klis, M.: The X-ray modulation of CYG X-3. A&A **101**, 299–304 (1981)

[47] Mason, K.O., Cordova, F.A., White, N.E.: Simultaneous X-Ray and Infrared Observations of Cygnus X-3. ApJ **309**, 700 (1986). https://doi.org/10.1086/164638

[48] Zdziarski, A.A., Malyshev, D., Dubus, G., Pooley, G.G., Johnson, T., Frankowski, A., De Marco, B., Chernyakova, M., Rao, A.R.: A comprehensive study of high-energy gamma-ray and radio emission from Cyg X-3. MNRAS **479**(4), 4399–4415 (2018) arXiv:1804.07460 [astro-ph.HE]. https://doi.org/10.1093/mnras/sty1618

[49] Stark, M.J., Saia, M.: Doppler Modulation of X-Ray Lines in Cygnus X-3. ApJ **587**(2), 101–104 (2003) arXiv:astro-ph/0301554 [astro-ph]. https://doi.org/10.1086/375287

[50] Willingale, R., King, A.R., Pounds, K.A.: EXOSAT MEDA observations of Cygnus X-3. MNRAS **215**, 295–314 (1985). https://doi.org/10.1093/mnras/215.3.295

[51] Poutanen, J., Nagendra, K.N., Svensson, R.: Green's matrix for Compton reflection of polarized radiation from cold matter. MNRAS **283**(3), 892–904 (1996). https://doi.org/10.1093/mnras/283.3.892

[52] Axelsson, M., Larsson, S., Hjalmarsdotter, L.: The aperiodic broad-band X-ray variability of Cygnus X-3. MNRAS **394**(3), 1544–1550 (2009) arXiv:0902.4007 [astro-ph.HE]. https://doi.org/10.1111/j.1365-2966.2009.14434.x

[53] Harrison, F.A., Craig, W.W., Christensen, F.E., Hailey, C.J., Zhang, W.W., Boggs, S.E., Stern, D., Cook, W.R., Forster, K., Giommi, P.: The Nuclear Spectroscopic Telescope Array (NuSTAR) High-energy X-Ray Mission. ApJ **770**(2), 103 (2013) arXiv:1301.7307 [astro-ph.IM]. https://doi.org/10.1088/0004-637X/770/2/103

[54] Sunyaev, R., Arefiev, V., Babyshkin, V., Bogomolov, A., Borisov, K., Buntov, M., Brunner, H., Burenin, R., Churazov, E., Coutinho, D., Eder, J., Eismont, N., Freyberg, M., Gilfanov, M., Gureyev, P., Hasinger, G., Khabibullin, I., Kolmykov, V., Komovkin, S., Krivonos, R., Lapshov, I., Levin, V., Lomakin, I., Lutovinov, A., Medvedev, P., Merloni, A., Mernik, T., Mikhailov, E., Molodtsov, V., Mzhelsky, P., Müller, S., Nandra, K., Nazarov, V., Pavlinsky, M., Poghodin, A., Predehl, P., Robrade, J., Sazonov, S., Scheuerle, H., Shirshakov, A., Tkachenko, A., Voron, V.: SRG X-ray orbital observatory. Its telescopes and first scientific results. A&A **656**, 132 (2021) arXiv:2104.13267 [astro-ph.HE]. https://doi.org/10.1051/0004-6361/202141179

[55] Pavlinsky, M., Tkachenko, A., Levin, V., Alexandrovich, N., Arefiev, V., Babyshkin, V., Batanov, O., Bodnar, Y., Bogomolov, A., Bubnov, A., Buntov, M., Burenin, R., Chelovekov, I., Chen, C.-T., Drozdova, T., Ehlert, S., Filippova, E., Frolov, S., Gamkov, D., Garanin, S., Garin, M., Glushenko, A., Gorelov, A., Grebenev, S., Grigorovich, S., Gureev, P., Gurova, E., Ilkaev, R., Katasonov, I., Krivchenko, A., Krivonos, R., Korotkov, F., Kudelin, M., Kuznetsova, M., Lazarchuk, V., Lomakin, I., Lapshov, I., Lipilin, V., Lutovinov, A., Mereminskiy, I., Molkov, S., Nazarov, V., Oleinikov, V., Pikalov, E., Ramsey, B.D., Roiz, I., Rotin, A., Ryadov, A., Sankin, E., Sazonov, S., Sedov, D., Semena, A., Semena, N., Serbinov, D., Shirshakov, A., Shtykovsky, A., Shvetsov, A., Sunyaev, R., Swartz, D.A., Tambov, V., Voron, V., Yaskovich, A.: The ART-XC telescope on board the SRG observatory. A&A **650**, 42 (2021) arXiv:2103.12479 [astro-ph.HE]. https://doi.org/10.1051/0004-6361/202040265

[56] Ubertini, P., Bazzano, A., Cocchi, M., Natalucci, L., Heise, J., Muller, J.M., in 't Zand, J.J.M.: Bursts from GS 1826-238: A Clocked Thermonuclear Flashes Generator. ApJ **514**(1), 27–30 (1999) arXiv:astro-ph/9901413 [astro-ph]. https://doi.org/10.1086/311933

[57] Lebrun, F., Leray, J.P., Lavocat, P., Crétolle, J., Arquès, M., Blondel, C., Bonnin, C., Bouère, A., Cara, C., Chaleil, T., Daly, F., Desages, F.,

Dzitko, H., Horeau, B., Laurent, P., Limousin, O., Mathy, F., Mauguen, V., Meignier, F., Molinié, F., Poindron, E., Rouger, M., Sauvageon, A., Tourrette, T.: ISGRI: The INTEGRAL Soft Gamma-Ray Imager. A&A **411**, 141–148 (2003) arXiv:astro-ph/0310362 [astro-ph]. https://doi.org/10.1051/0004-6361:20031367

[58] Courvoisier, T.J.-L., Walter, R., Beckmann, V., Dean, A.J., Dubath, P., Hudec, R., Kretschmar, P., Mereghetti, S., Montmerle, T., Mowlavi, N., Paltani, S., Preite Martinez, A., Produit, N., Staubert, R., Strong, A.W., Swings, J.-P., Westergaard, N.J., White, N., Winkler, C., Zdziarski, A.A.: The INTEGRAL Science Data Centre (ISDC). A&A **411**, 53–57 (2003) arXiv:astro-ph/0308047 [astro-ph]. https://doi.org/10.1051/0004-6361:20031172

[59] Neronov, A., Savchenko, V., Tramacere, A., Meharga, M., Ferrigno, C., Paltani, S.: Online data analysis system of the INTEGRAL telescope. A&A **651**, 97 (2021) arXiv:2002.12895 [astro-ph.IM]. https://doi.org/10.1051/0004-6361/202037850

[60] Mattox, J.R., Bertsch, D.L., Chiang, J., Dingus, B.L., Digel, S.W., Esposito, J.A., Fierro, J.M., Hartman, R.C., Hunter, S.D., Kanbach, G., Kniffen, D.A., Lin, Y.C., Macomb, D.J., Mayer-Hasselwander, H.A., Michelson, P.F., von Montigny, C., Mukherjee, R., Nolan, P.L., Ramana-murthy, P.V., Schneid, E., Sreekumar, P., Thompson, D.J., Willis, T.D.: The Likelihood Analysis of EGRET Data. ApJ **461**, 396 (1996). https://doi.org/10.1086/177068

[61] Atwood, W., Albert, A., Baldini, L., Tinivella, M., Bregeon, J., Pesce-Rollins, M., Sgrò, C., Bruel, P., Charles, E., Drlica-Wagner, A., Franck-owiak, A., Jogler, T., Rochester, L., Usher, T., Wood, M., Cohen-Tanugi, J., Zimmer, S.: Pass 8: Toward the Full Realization of the Fermi-LAT Scientific Potential. arXiv e-prints, 1303–3514 (2013) arXiv:1303.3514 [astro-ph.IM]. https://doi.org/10.48550/arXiv.1303.3514

[62] Abdollahi, S., Acero, F., Ackermann, M., Ajello, M., Atwood, W.B., Axelsson, M., Baldini, L., Ballet, J., Barbiellini, G., Bastieri, D., Becerra Gonzalez, J., Bellazzini, R., Berretta, A., Bissaldi, E., Bland ford, R.D., Bloom, E.D., Bonino, R., Bottacini, E., Brandt, T.J., Bregeon, J., Bruel, P., Buehler, R., Burnett, T.H., Buson, S., Cameron, R.A., Caputo, R., Caraveo, P.A., Casandjian, J.M., Castro, D., Cavazzuti, E., Charles, E., Chaty, S., Chen, S., Cheung, C.C., Chiaro, G., Ciprini, S., Cohen-Tanugi, J., Cominsky, L.R., Coronado-Blázquez, J., Costantin, D., Cuoco, A., Cutini, S., D'Ammando, F., DeKlotz, M., de la Torre Luque, P., de Palma, F., Desai, A., Digel, S.W., Di Lalla, N., Di Mauro, M., Di Venere, L., Domínguez, A., Dumora, D., Fana Dirirsa, F., Fegan, S.J., Fer-rara, E.C., Franckowiak, A., Fukazawa, Y., Funk, S., Fusco, P., Gargano,

F., Gasparrini, D., Giglietto, N., Giommi, P., Giordano, F., Giroletti, M., Glanzman, T., Green, D., Grenier, I.A., Griffin, S., Grondin, M.-H., Grove, J.E., Guiriec, S., Harding, A.K., Hayashi, K., Hays, E., Hewitt, J.W., Horan, D., Jóhannesson, G., Johnson, T.J., Kamae, T., Kerr, M., Kocevski, D., Kovac'evic', M., Kuss, M., Landriu, D., Larsson, S., Latronico, L., Lemoine-Goumard, M., Li, J., Liodakis, I., Longo, F., Loparco, F., Lott, B., Lovellette, M.N., Lubrano, P., Madejski, G.M., Maldera, S., Malyshev, D., Manfreda, A., Marchesini, E.J., Marcotulli, L., Martí-Devesa, G., Martin, P., Massaro, F., Mazziotta, M.N., McEnery, J.E., Mereu, I., Meyer, M., Michelson, P.F., Mirabal, N., Mizuno, T., Monzani, M.E., Morselli, A., Moskalenko, I.V., Negro, M., Nuss, E., Ojha, R., Omodei, N., Orienti, M., Orlando, E., Ormes, J.F., Palatiello, M., Paliya, V.S., Paneque, D., Pei, Z., Peña-Herazo, H., Perkins, J.S., Persic, M., Pesce-Rollins, M., Petrosian, V., Petrov, L., Piron, F., Poon, H., Porter, T.A., Principe, G., Rainò, S., Rando, R., Razzano, M., Razzaque, S., Reimer, A., Reimer, O., Remy, Q., Reposeur, T., Romani, R.W., Saz Parkinson, P.M., Schinzel, F.K., Serini, D., Sgrò, C., Siskind, E.J., Smith, D.A., Spandre, G., Spinelli, P., Strong, A.W., Suson, D.J., Tajima, H., Takahashi, M.N., Tak, D., Thayer, J.B., Thompson, D.J., Tibaldo, L., Torres, D.F., Torresi, E., Valverde, J., Van Klaveren, B., van Zyl, P., Wood, K., Yassine, M., Zaharijas, G.: Fermi Large Area Telescope Fourth Source Catalog. ApJS **247**(1), 33 (2020) arXiv:1902.10045 [astro-ph.HE]. https://doi.org/10.3847/1538-4365/ab6bcb

[63] Tavani, M., Barbiellini, G., Argan, A., Boffelli, F., Bulgarelli, A., Caraveo, P., Cattaneo, P.W., Chen, A.W., Cocco, V., Costa, E., D'Ammando, F., Del Monte, E., de Paris, G., Di Cocco, G., di Persio, G., Donnarumma, I., Evangelista, Y., Feroci, M., Ferrari, A., Fiorini, M., Fornari, F., Fuschino, F., Froysland, T., Frutti, M., Galli, M., Gianotti, F., Giuliani, A., Labanti, C., Lapshov, I., Lazzarotto, F., Liello, F., Lipari, P., Longo, F., Mattaini, E., Marisaldi, M., Mastropietro, M., Mauri, A., Mauri, F., Mereghetti, S., Morelli, E., Morselli, A., Pacciani, L., Pellizzoni, A., Perotti, F., Piano, G., Picozza, P., Pontoni, C., Porrovecchio, G., Prest, M., Pucella, G., Rapisarda, M., Rappoldi, A., Rossi, E., Rubini, A., Soffitta, P., Traci, A., Trifoglio, M., Trois, A., Vallazza, E., Vercellone, S., Vittorini, V., Zambra, A., Zanello, D., Pittori, C., Preger, B., Santolamazza, P., Verrecchia, F., Giommi, P., Colafrancesco, S., Antonelli, A., Cutini, S., Gasparrini, D., Stellato, S., Fanari, G., Primavera, R., Tamburelli, F., Viola, F., Guarrera, G., Salotti, L., D'Amico, F., Marchetti, E., Crisconio, M., Sabatini, P., Annoni, G., Alia, S., Longoni, A., Sanquerin, R., Battilana, M., Concari, P., Dessimone, E., Grossi, R., Parise, A., Monzani, F., Artina, E., Pavesi, R., Marseguerra, G., Nicolini, L., Scandelli, L., Soli, L., Vettorello, V., Zardetto, E., Bonati, A., Maltecca, L., D'Alba, E., Patané, M., Babini, G., Onorati, F., Acquaroli, L., Angelucci, M., Morelli, B., Agostara, C., Cerone, M., Michetti, A., Tempesta, P., D'Eramo, S., Rocca, F., Giannini, F., Borghi, G., Garavelli, B.,

Conte, M., Balasini, M., Ferrario, I., Vanotti, M., Collavo, E., Giacomazzo, M.: The AGILE Mission. A&A **502**(3), 995–1013 (2009) arXiv:0807.4254 [astro-ph]. https://doi.org/10.1051/0004-6361/200810527

[64] Pittori, C.: The AGILE data center and its legacy. Rendiconti Lincei. Scienze Fisiche e Naturali **30**, 217–223 (2019) arXiv:1911.12314 [astro-ph.IM]. https://doi.org/10.1007/s12210-019-00857-x

[65] Bulgarelli, A., Chen, A.W., Tavani, M., Gianotti, F., Trifoglio, M., Contessi, T.: Evaluating the maximum likelihood method for detecting short-term variability of AGILE γ-ray sources. A&A **540**, 79 (2012) arXiv:1201.2602 [astro-ph.IM]. https://doi.org/10.1051/0004-6361/201118023

[66] Bulgarelli, A., Fioretti, V., Parmiggiani, N., Verrecchia, F., Pittori, C., Lucarelli, F., Tavani, M., Aboudan, A., Cardillo, M., Giuliani, A., Cattaneo, P.W., Chen, A.W., Piano, G., Rappoldi, A., Baroncelli, L., Argan, A., Antonelli, L.A., Donnarumma, I., Gianotti, F., Giommi, P., Giusti, M., Longo, F., Pellizzoni, A., Pilia, M., Trifoglio, M., Trois, A., Vercellone, S., Zoli, A.: Second AGILE catalogue of gamma-ray sources. A&A **627**, 13 (2019) arXiv:1903.06957 [astro-ph.HE]. https://doi.org/10.1051/0004-6361/201834143

[67] Zwart, J.T.L., Barker, R.W., Biddulph, P., Bly, D., Boysen, R.C., Brown, A.R., Clementson, C., Crofts, M., Culverhouse, T.L., Czeres, J., Dace, R.J., Davies, M.L., D'Alessandro, R., Doherty, P., Duggan, K., Ely, J.A., Felvus, M., Feroz, F., Flynn, W., Franzen, T.M.O., Geisbüsch, J., Génova-Santos, R., Grainge, K.J.B., Grainger, W.F., Hammett, D., Hills, R.E., Hobson, M.P., Holler, C.M., Hurley-Walker, N., Jilley, R., Jones, M.E., Kaneko, T., Kneissl, R., Lancaster, K., Lasenby, A.N., Marshall, P.J., Newton, F., Norris, O., Northrop, I., Odell, D.M., Petencin, G., Pober, J.C., Pooley, G.G., Pospieszalski, M.W., Quy, V., Rodríguez-Gonzálvez, C., Saunders, R.D.E., Scaife, A.M.M., Schofield, J., Scott, P.F., Shaw, C., Shimwell, T.W., Smith, H., Taylor, A.C., Titterington, D.J., Velić, M., Waldram, E.M., West, S., Wood, B.A., Yassin, G., AMI Consortium: The Arcminute Microkelvin Imager. MNRAS **391**(4), 1545–1558 (2008). https://doi.org/10.1111/j.1365-2966.2008.13953.x

[68] Hickish, J., Razavi-Ghods, N., Perrott, Y.C., Titterington, D.J., Carey, S.H., Scott, P.F., Grainge, K.J.B., Scaife, A.M.M., Alexander, P., Saunders, R.D.E., Crofts, M., Javid, K., Rumsey, C., Jin, T.Z., Ely, J.A., Shaw, C., Northrop, I.G., Pooley, G., D'Alessandro, R., Doherty, P., Willatt, G.P.: A digital correlator upgrade for the Arcminute MicroKelvin Imager. MNRAS **475**(4), 5677–5687 (2018). https://doi.org/10.1093/mnras/sty074

[69] Ott, M., Witzel, A., Quirrenbach, A., Krichbaum, T.P., Standke, K.J., Schalinski, C.J., Hummel, C.A.: An updated list of radio flux density calibrators. A&A **284**, 331–339 (1994)

[70] Egron, E., Pellizzoni, A., Giroletti, M., Righini, S., Stagni, M., Orlati, A., Migoni, C., Melis, A., Concu, R., Barbas, L., Buttaccio, S., Cassaro, P., De Vicente, P., Gawroński, M.P., Lindqvist, M., Maccaferri, G., Stanghellini, C., Wolak, P., Yang, J., Navarrini, A., Loru, S., Pilia, M., Bachetti, M., Iacolina, M.N., Buttu, M., Corbel, S., Rodriguez, J., Markoff, S., Wilms, J., Pottschmidt, K., Cadolle Bel, M., Kalemci, E., Belloni, T., Grinberg, V., Marongiu, M., Vargiu, G.P., Trois, A.: Single-dish and VLBI observations of Cygnus X-3 during the 2016 giant flare episode. MNRAS **471**(3), 2703–2714 (2017) arXiv:1707.03761 [astro-ph.HE]. https://doi.org/10.1093/mnras/stx1730

[71] Tsybulev, P.G., Nizhelskii, N.A., Dugin, M.V., Borisov, A.N., Kratov, D.V., Udovitskii, R.Y.: C-Band Radiometer for Continuum Observations at RATAN-600 Radio Telescope. Astrophysical Bulletin **73**(4), 494–500 (2018). https://doi.org/10.1134/S1990341318040132

[72] Kale, R., Ishwara-Chandra, C.H.: CAPTURE: a continuum imaging pipeline for the uGMRT. Experimental Astronomy **51**(1), 95–108 (2021) arXiv:2010.00196 [astro-ph.IM]. https://doi.org/10.1007/s10686-020-09677-6

[73] Marrone, D.P., Rao, R.: The submillimeter array polarimeter. In: Duncan, W.D., Holland, W.S., Withington, S., Zmuidzinas, J. (eds.) Millimeter and Submillimeter Detectors and Instrumentation for Astronomy IV. Society of Photo-Optical Instrumentation Engineers (SPIE) Conference Series, vol. 7020, p. 70202 (2008). https://doi.org/10.1117/12.788677

[74] Chandrasekhar, S.: Radiative Transfer. Dover, New York (1960)

[75] Goosmann, R.W., Gaskell, C.M.: Modeling optical and UV polarization of AGNs. I. Imprints of individual scattering regions. A&A **465**(1), 129–145 (2007) arXiv:astro-ph/0507072 [astro-ph]. https://doi.org/10.1051/0004-6361:20053555

[76] Marin, F., Dovčiak, M., Muleri, F., Kislat, F.F., Krawczynski, H.S.: Predicting the X-ray polarization of type 2 Seyfert galaxies. MNRAS **473**(1), 1286–1316 (2018) arXiv:1709.03304 [astro-ph.HE]. https://doi.org/10.1093/mnras/stx2382

[77] Asplund, M., Grevesse, N., Sauval, A.J.: The Solar Chemical Composition. In: Barnes, I. Thomas G., Bash, F.N. (eds.) Cosmic Abundances as Records of Stellar Evolution and Nucleosynthesis. Astronomical Society of the Pacific Conference Series, vol. 336, p. 25 (2005)

[78] Magdziarz, P., Zdziarski, A.A.: Angle-dependent Compton reflection of X-rays and gamma-rays. MNRAS **273**(3), 837–848 (1995). https://doi.org/10.1093/mnras/273.3.837

[79] Miller-Jones, J.C.A., Bahramian, A., Orosz, J.A., Mandel, I., Gou, L., Maccarone, T.J., Neijssel, C.J., Zhao, X., Ziółkowski, J., Reid, M.J., Uttley, P., Zheng, X., Byun, D.-Y., Dodson, R., Grinberg, V., Jung, T., Kim, J.-S., Marcote, B., Markoff, S., Rioja, M.J., Rushton, A.P., Russell, D.M., Sivakoff, G.R., Tetarenko, A.J., Tudose, V., Wilms, J.: Cygnus X-1 contains a 21-solar mass black hole—Implications for massive star winds. Science **371**(6533), 1046–1049 (2021) arXiv:2102.09091 [astro-ph.HE]. https://doi.org/10.1126/science.abb3363

[80] King, A.R.: Masses, beaming and Eddington ratios in ultraluminous X-ray sources. MNRAS **393**(1), 41–44 (2009) arXiv:0811.1473 [astro-ph]. https://doi.org/10.1111/j.1745-3933.2008.00594.x

[81] Mushtukov, A.A., Portegies Zwart, S.: Bright X-ray pulsars: how outflows influence beaming, pulsations and pulse phase lags. MNRAS **518**(4), 5457–5464 (2023) arXiv:2211.08952 [astro-ph.HE]. https://doi.org/10.1093/mnras/stac3431